

Scalable Bayesian transport maps for high-dimensional non-Gaussian spatial fields

Matthias Katzfuss*

Florian Schäfer†

Abstract

A multivariate distribution can be described by a triangular transport map from the target distribution to a simple reference distribution. We propose Bayesian non-parametric inference on the transport map by modeling its components using Gaussian processes. This enables regularization and accounting for uncertainty in the map estimation, while still resulting in a closed-form and invertible posterior map. We then focus on inferring the distribution of a nonstationary spatial field from a small number of replicates. We develop specific transport-map priors that are highly flexible but shrink toward a Gaussian field with Matérn-type covariance. The approach is scalable to high-dimensional fields due to data-dependent sparsity and parallel computations. We also discuss extensions, including Dirichlet process mixtures for marginal non-Gaussianity. We present numerical results to demonstrate the accuracy, scalability, and usefulness of our methods, including statistical emulation of non-Gaussian climate-model output.

Keywords: climate-model emulation; Dirichlet process mixture; Gaussian process; maximin ordering; nonstationarity; sparse triangular transport

1 Introduction

Inference on a high-dimensional joint distribution based on a relatively small number of replicates is important in many applications, such as in ensemble-based data assimilation and in the analysis of geospatial data and functional computer-model output. An important example is statistical climate-model emulation (e.g., Castruccio et al., 2014; Nychka et al., 2018; Haugen et al., 2019), whose goal is to learn a high-dimensional, nonstationary, and non-Gaussian spatial distribution from an ensemble of spatial fields generated by an expensive computer model (see Figure 1).

Existing methods for spatial inference are often geared toward a single training replicate, assuming Gaussian processes (GPs) with simple parametric covariance functions (e.g., Cressie, 1993; Banerjee et al., 2004). Many extensions to nonstationary (e.g., as reviewed by Risser, 2016) or nonparametric covariances (e.g., Huang et al., 2011; Choi et al., 2013; Porcu

*Department of Statistics, Texas A&M University. Corresponding author: katzfuss@gmail.com

†School of Computational Science and Engineering, Georgia Institute of Technology

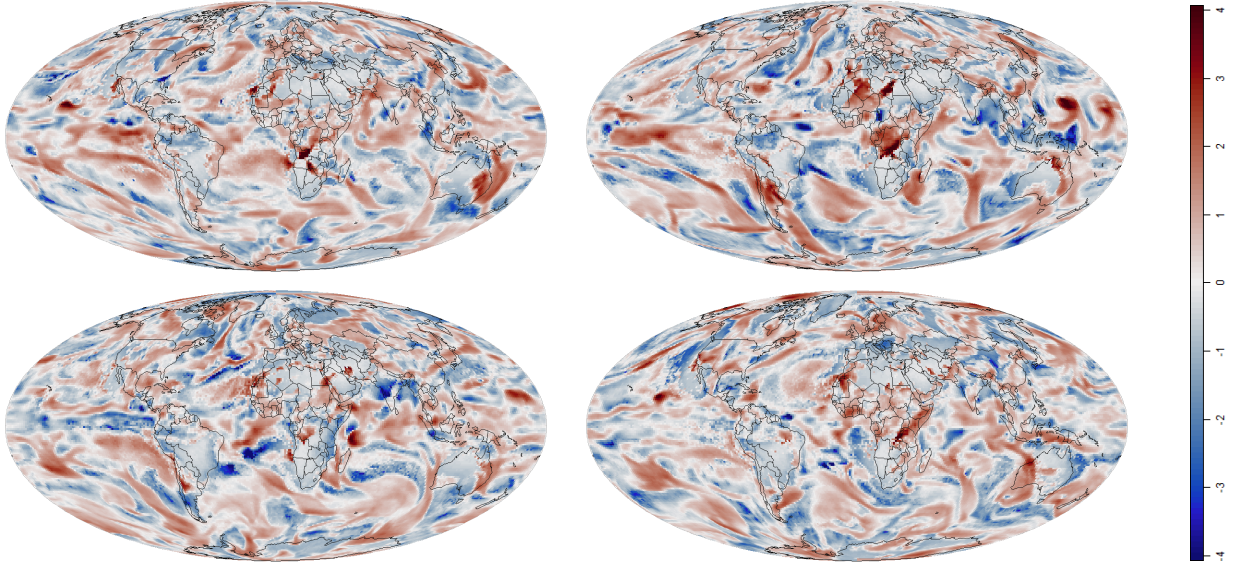


Figure 1: Four members of an ensemble of log-transformed precipitation anomalies produced by a climate model, on a global grid of size $N = 288 \times 192 = 55,296$. We want to infer the N -dimensional distribution based on a small ensemble of size $n < 100$. See Section 6 for details.

et al., 2019) have been proposed, but these typically still rely on implicit or explicit assumptions of Gaussianity. For non-Gaussian spatial data, GPs can be transformed or used as latent building blocks (see, e.g., Gelfand and Schliep, 2016; Xu and Genton, 2017, and references therein), but relying only on a GP’s covariance function limits the types of dependence that can be captured. Parametric non-Gaussian Matérn fields can be constructed using stochastic partial differential equations driven by non-Gaussian noise (Wallin and Bolin, 2015; Bolin and Wallin, 2020). Models for non-Gaussian spatial data can also be built using copulas; for example, Gräler (2014) proposed vine copulas for spatial fields with extremal behavior, and the factor copula approach of Krupskii et al. (2018) assumes all locations in a homogeneous spatial region to be affected by a common latent factor. Many existing non-Gaussian spatial methods are not scalable to large datasets without approximations.

A convenient and flexible way to model a continuous multivariate distribution with any dependence structure is via a triangular transport map (see Marzouk et al., 2016, for a review) that transforms the target distribution to a reference distribution (e.g., standard Gaussian). For Gaussian distributions, such a map is linear and given by the Cholesky factor of the precision matrix; non-Gaussian distributions can be obtained by allowing nonlinearities in the map. Given an invertible transport map, it is straightforward to sample from the target distribution and some of its conditionals, or to transform the non-Gaussian data to the reference space, in which simple linear operations (e.g., averaging) may be more meaningful. Typically, the map is estimated based on training data, often by iteratively expanding a finite-dimensional parameterization of the transport map (e.g., El Moselhy and Marzouk, 2012; Bigoni et al., 2016; Marzouk et al., 2016; Baptista et al., 2020); subsequent inference is then carried out assuming that the map is known.

Here we propose Bayesian inference on a transport map that describes a multivariate continuous distribution and is learned from a limited number of samples from the distri-

bution. We model the map components using nonparametric, conjugate Gaussian-process priors, which probabilistically regularize the map and shrink toward linearity. The resulting procedure is flexible, naturally quantifies uncertainty, and adjusts to the amount of complexity that is discernible from the training data, thus avoid both over- and under-fitting. The conjugacy results in simple, closed-form inference. Instead of assuming Gaussianity for the multivariate target distribution, our approach is equivalent to a series of conditional GP regression problems that together characterize a non-Gaussian target distribution.

We then focus on the case of a spatial target distribution, for which the dimension (i.e., the number of spatial locations) is high and the number of training replicates is relatively small. In this setting, our Bayesian transport maps impose sparsity and regularization motivated by the behavior of diffusion-type processes prevalent in many environmental applications. After applying a so-called maximin ordering of the spatial locations, determining the triangular transport map essentially consists of conditional spatial-prediction problems on an increasingly fine scale. The screening effect prevalent for many spatial processes leads to a decay of influence that allows us to only consider nearby observations in these prediction problems. In addition, as the scale decreases in a systematic way in the maximin ordering, we can implicitly shrink toward linear Gaussian Matérn type models. The resulting Bayesian methods scale near-linearly in the number of spatial locations, and the main computations are trivially parallel. Hyperparameters, which are estimated from the data, determine the amount of shrinkage and sparsity. As a special case, the hyperparameters can be set such set the transport map is forced to be linear and is essentially equivalent to a sparse inverse Cholesky factor of the precision matrix; the joint distribution then becomes Gaussian, and we obtain a model very similar to that in Kidd and Katzfuss (2021), who proposed flexible Bayesian methods for inferring the covariance matrix of a Gaussian spatial field based on a sparse Cholesky factor of the precision matrix.

We extend this approach to further increase the flexibility in the (continuous) marginal distributions by modeling the GP-regression error terms using Dirichlet process mixtures, which can be fit using a Gibbs sampler. Our approach lets the data decide the degrees of nonlinearity, nonstationary, and non-Gaussianity, with little to no manual tuning or model-selection required. We also discuss an extension for settings in which Euclidean distance between the locations is not meaningful or in which variables are not identified by spatial locations (e.g., multivariate spatial processes).

The remainder of this document is organized as follows. In Section 2, we develop Bayesian transport maps. In Section 3, we consider the special case of high-dimensional spatial distributions. In Section 4, we discuss extensions to non-Gaussian marginals using Dirichlet process mixtures. Sections 5 and 6 provide comparisons and applications to simulated data and climate-model output, respectively. Section 7 concludes and discusses future work. Appendices A and C contain proofs and details on fitting the model with Dirichlet process mixtures. R code to run our method and reproduce all results is available at <https://github.com/katzfuss-group/BaTraMaSpa>.

2 Bayesian transport maps

2.1 Transport maps as regressions

Consider a continuous random vector $\mathbf{y} = (y_1, \dots, y_N)^\top$, for example describing a spatial field at N locations as in Figure 1. For simplicity, assume that \mathbf{y} has been centered to have mean zero.

For a multivariate Gaussian distribution, $\mathbf{y} \sim \mathcal{N}_N(\mathbf{0}, \Sigma)$ with $\Sigma^{-1} = \mathbf{L}^\top \mathbf{L}$, the (lower-triangular) Cholesky factor \mathbf{L} represents a transformation to a standard normal: $\mathbf{z} = \mathbf{L}\mathbf{y} \sim \mathcal{N}_N(\mathbf{0}, \mathbf{I}_N)$. As a natural extension, we can characterize any continuous N -variate distribution $p(\mathbf{y})$ by a potentially nonlinear transport map $\mathcal{T} : \mathbb{R}^N \rightarrow \mathbb{R}^N$ (Villani, 2009), such that $\mathbf{z} = \mathcal{T}(\mathbf{y}) \sim \mathcal{N}_N(\mathbf{0}, \mathbf{I}_N)$ for $\mathbf{y} \sim p(\mathbf{y})$. Like \mathbf{L} , we can assume without loss of generality that the transport map \mathcal{T} is lower-triangular (Rosenblatt, 1952; Carlier et al., 2009),

$$\mathcal{T}(\mathbf{y}) = \begin{bmatrix} \mathcal{T}_1(y_1) \\ \mathcal{T}_2(y_1, y_2) \\ \vdots \\ \mathcal{T}_N(y_1, y_2, \dots, y_N) \end{bmatrix}, \quad (1)$$

where each $\mathcal{T}_i(\mathbf{y}_{1:i})$ with $\mathbf{y}_{1:i} = (y_1, \dots, y_i)^\top$ is an increasing function of its i th argument. Letting $\mathcal{N}(x|\mu, \sigma^2)$ denote a Gaussian density with parameters μ and σ^2 evaluated at x , we then have

$$p(\mathbf{y}) = p_{\mathbf{z}}(\mathcal{T}(\mathbf{y})) |\det \nabla \mathcal{T}| = \prod_{i=1}^N \left(\mathcal{N}(\mathcal{T}_i(\mathbf{y}_{1:i})|0, 1) \left| \frac{\partial \mathcal{T}_i(\mathbf{y}_{1:i})}{\partial y_i} \right| \right), \quad (2)$$

as the triangular \mathcal{T} also implies a triangular $\nabla \mathcal{T} = (\frac{\partial \mathcal{T}_i(\mathbf{y}_{1:i})}{\partial y_j})_{i,j=1,\dots,N}$.

Throughout, we assume each \mathcal{T}_i to be additive in its i th argument,

$$\mathcal{T}_i(\mathbf{y}_{1:i}) = (y_i - f_i(\mathbf{y}_{1:i-1}))/d_i, \quad i = 1, \dots, N, \quad (3)$$

where $d_i \in \mathbb{R}^+$, $f_i : \mathbb{R}^{i-1} \rightarrow \mathbb{R}$ for $i = 2, \dots, n$, and $f_i(\mathbf{y}_{1:i-1}) \equiv 0$ for $i = 1$. Then, $\partial_i \mathcal{T}_i(\mathbf{y}_{1:i}) = 1/d_i > 0$, as required. Using (2), it is easy to show that

$$p(\mathbf{y}) \propto \prod_{i=1}^N \left(\exp(-\frac{1}{2d_i^2}(y_i - f_i(\mathbf{y}_{1:i-1}))^2) \frac{1}{d_i} \right) \propto \prod_{i=1}^N \mathcal{N}(y_i|f_i(\mathbf{y}_{1:i-1}), d_i^2). \quad (4)$$

Thus, the transport-map approach has turned the difficult problem of inferring the N -variate distribution of \mathbf{y} into N independent regressions of y_i on $\mathbf{y}_{1:i-1}$ of the form

$$y_i = f(\mathbf{y}_{1:i-1}) + \epsilon_i, \quad \epsilon_i \sim \mathcal{N}(0, d_i^2), \quad i = 1, \dots, N. \quad (5)$$

2.2 Modeling the map functions using Gaussian processes

In the existing transport-map literature (e.g., Marzouk et al., 2016), $f_i : \mathbb{R}^{i-1} \rightarrow \mathbb{R}$ and $d_i \in \mathbb{R}^+$ in (3)–(5) are often assumed to have parametric form, whose parameters are estimated and then assumed known. Instead, we here assume a flexible, nonparametric prior on the map \mathcal{T} by specifying independent conjugate Gaussian-process-inverse-Gamma priors for the f_i and d_i^2 . These prior assumptions induce prior distributions on the map components \mathcal{T}_i in

(3), and thus on the entire map \mathcal{T} in (1). Our Bayesian model is most appropriate when the y_i are or have been transformed to be marginally Gaussian, but this will be relaxed in Section 4.

Specifically, for the “noise” variances d_i^2 , we assume inverse-Gamma distributions,

$$d_i^2 \stackrel{\text{ind.}}{\sim} \mathcal{IG}(\alpha_i, \beta_i), \quad i = 1, \dots, N. \quad (6)$$

Conditional on d_i^2 , each function f_i is modeled as a Gaussian process (GP). We implicitly assume a linear mean for the GP, but by using a Gaussian prior distribution for the linear coefficients, we can absorb the mean into the covariance function. This results in a zero-mean GP,

$$f_i | d_i \stackrel{\text{ind.}}{\sim} \mathcal{GP}(0, d_i^2 K_i), \quad i = 1, \dots, N, \quad (7)$$

where we multiply the kernel function by d_i^2 for conjugacy and then counteract by dividing $K_i(\cdot, \cdot) = C_i(\cdot, \cdot)/E(d_i^2)$ by $E(d_i^2) = \beta_i/(\alpha_i - 1)$. Due to absorbing the GP mean into the kernel, the covariance function

$$C_i(\mathbf{y}_{1:i-1}, \mathbf{y}'_{1:i-1}) = \mathbf{y}_{1:i-1}^\top \mathbf{Q}_i \mathbf{y}'_{1:i-1} + \sigma_i^2 \rho_i(\mathbf{y}_{1:i-1}, \mathbf{y}'_{1:i-1}), \quad i = 1, \dots, N, \quad (8)$$

consists of a linear component and of a nonlinear component with a positive-definite correlation function ρ_i , such that $\rho_i(\mathbf{y}_{1:i-1}, \mathbf{y}_{1:i-1}) = 1$. The factor σ_i^2 determines the degree of nonlinearity; if $\sigma_i^2 = 0$, then f_i becomes a linear function of $\mathbf{y}_{1:i-1}$.

The prior distributions (i.e., α_i , β_i , K_i) may depend on hyperparameters $\boldsymbol{\theta}$; see Section 2.4 for more details.

2.3 The posterior map

Now assume that we have observed n independent training samples $\mathbf{y}^{(1)}, \dots, \mathbf{y}^{(n)}$ from the distribution in Section 2.1 conditional on $\mathbf{f} = (f_1, \dots, f_N)$ and $\mathbf{d} = (d_1, \dots, d_N)$, such that $\mathbf{y}^{(j)} \stackrel{\text{iid}}{\sim} p(\mathbf{y} | \mathbf{f}, \mathbf{d})$ with $\mathcal{T}(\mathbf{y}^{(j)}) | \mathbf{f}, \mathbf{d} \sim \mathcal{N}_N(\mathbf{0}, \mathbf{I}_N)$, $j = 1, \dots, n$. We combine the samples into a $n \times N$ data matrix \mathbf{Y} whose j th row is given by $\mathbf{y}^{(j)}$. Then, for the regression in (5), the responses \mathbf{y}_i and the covariates $\mathbf{Y}_{1:i-1}$ are given by the i th and the first $i-1$ columns of \mathbf{Y} , respectively. Below, let \mathbf{y}^* denote a new observation sampled from the same distribution, $\mathbf{y}^* \sim p(\mathbf{y} | \mathbf{f}, \mathbf{d})$, independently of \mathbf{Y} .

Based on the prior distribution for \mathbf{f} and \mathbf{d} in Section 2.2, we can now determine the posterior map $\tilde{\mathcal{T}}$ learned from the training data \mathbf{Y} , with \mathbf{f} and \mathbf{d} integrated out. This map is available in closed form and invertible:

PROPOSITION 1. *The transport map $\tilde{\mathcal{T}}$ from $\mathbf{y}^* \sim p(\mathbf{y} | \mathbf{Y})$ to $\mathbf{z}^* = \tilde{\mathcal{T}}(\mathbf{y}^*) \sim \mathcal{N}_N(\mathbf{0}, \mathbf{I}_N)$ is a triangular map with components*

$$z_i^* = \tilde{\mathcal{T}}_i(y_1^*, \dots, y_i^*) = \Phi^{-1}\left(F_{2\tilde{\alpha}_i}\left(\hat{d}_i^{-1}(v_i(\mathbf{y}_{1:i-1}^*) + 1)^{-1/2}(y_i^* - \hat{f}_i(\mathbf{y}_{1:i-1}^*))\right)\right), \quad i = 1, \dots, N, \quad (9)$$

where $\tilde{\alpha}_i = \alpha_i + n/2$, $\tilde{\beta}_i = \beta_i + \mathbf{y}_i^\top \mathbf{G}_i^{-1} \mathbf{y}_i/2$, $\hat{d}_i^2 = \tilde{\beta}_i/\tilde{\alpha}_i$, $\mathbf{G}_i = \mathbf{K}_i + \mathbf{I}_n$,

$$\hat{f}_i(\mathbf{y}_{1:i-1}^*) = K_i(\mathbf{y}_{1:i-1}^*, \mathbf{Y}_{1:i-1}) \mathbf{G}_i^{-1} \mathbf{y}_i, \quad (10)$$

$$v_i(\mathbf{y}_{1:i-1}^*) = K_i(\mathbf{y}_{1:i-1}^*, \mathbf{y}_{1:i-1}^*) - K_i(\mathbf{y}_{1:i-1}^*, \mathbf{Y}_{1:i-1}) \mathbf{G}_i^{-1} K_i(\mathbf{Y}_{1:i-1}, \mathbf{y}_{1:i-1}^*), \quad (11)$$

for $i = 2, \dots, N$, $\hat{f}_1 = v_1 = 0$ for $i = 1$, and Φ and F_κ denote the cumulative distribution functions of the standard normal and the t distribution with κ degrees of freedom, respectively. The inverse map $\tilde{\mathcal{T}}^{-1}$ can be evaluated at a given \mathbf{z}^* by solving the nonlinear triangular system $\tilde{\mathcal{T}}(\mathbf{y}^*) = \mathbf{z}^*$ for \mathbf{y}^* ; because $\tilde{\mathcal{T}}$ is triangular, the solution can be expressed recursively as:

$$y_i^* = \hat{f}_i(\mathbf{y}_{1:i-1}^*) + F_{2\tilde{\alpha}_i}^{-1}(\Phi(z_i)) \hat{d}_i(v_i(\mathbf{y}_{1:i-1}^*) + 1)^{1/2}, \quad i = 1, \dots, N. \quad (12)$$

All proofs are provided in Appendix A. Note that we can also write the prior map in a similar form, but the prior map will only be useful in the case of highly informative priors.

Determining $\tilde{\mathcal{T}}_i$ requires $\mathcal{O}(n^3 + in^2)$ time, largely for computing and decomposing the $n \times n$ matrix \mathbf{G}_i , for each $i = 1, \dots, N$. However, note that the N rows or components of $\tilde{\mathcal{T}}$ can be computed completely in parallel, as in the optimization-based transport-map estimation reviewed in Marzouk et al. (2016). Each application of the transport map or its inverse then consists of the GP prediction in (10)–(11) and only requires $\mathcal{O}(n^2 + in)$ time for $i = 1, \dots, N$, but the inverse map is evaluated recursively (i.e., not in parallel).

In contrast to previous transport-map approaches, our approach is Bayesian and naturally quantifies uncertainty in the nonlinear transport functions. The GP priors on the f_i automatically adapt to the amount of information available, only resulting in strongly nonlinear function estimates when supplied the requisite evidence by the data. However, we can also consider some simple special cases. If n is increasing, then $\tilde{\alpha}_i$ increases, $F_{2\tilde{\alpha}_i}$ converges to Φ , and $v_i(\mathbf{y}_{1:i-1}^*)$ will typically converge to zero, and so the map components will simplify to

$$\tilde{\mathcal{T}}_i(y_1^*, \dots, y_i^*) = (y_i^* - \hat{f}_i(\mathbf{y}_{1:i-1}^*)) / \hat{d}_i \quad \text{and} \quad y_i^* = \hat{f}_i(\mathbf{y}_{1:i-1}^*) + z_i \hat{d}_i. \quad (13)$$

When employed for finite n , this simplified version of the map ignores posterior uncertainty in \mathbf{f} and \mathbf{d} and simply relies on the point estimates $\hat{f}_i(\mathbf{y}_{1:i-1})$ and \hat{d}_i^2 . For this simplified map, if we also assume that $\sigma_i = 0$ in (8) for all $i = 1, \dots, N$, then all f_i and all $\tilde{\mathcal{T}}_i$ will become linear functions; we can think of the resulting linear map $\tilde{\mathcal{T}}(\mathbf{y}^*) = \mathbf{L}^\top \mathbf{y}^*$ as an inverse Cholesky factor, in the sense that $\mathbf{y}^* | \mathbf{Y} \sim \mathcal{N}(\mathbf{0}, \mathbf{\Lambda}^{-1})$ with $\mathbf{\Lambda} = \mathbf{L}\mathbf{L}^\top$.

Transport maps can be used for a variety of purposes. For example, we can obtain a new sample \mathbf{y}^* from the posterior predictive distribution $p(\mathbf{y} | \mathbf{Y})$ by sampling $\mathbf{z} \sim \mathcal{N}_N(\mathbf{0}, \mathbf{I}_N)$ and then applying the inverse map $\tilde{\mathcal{T}}^{-1}$ in (12). The map $\tilde{\mathcal{T}}$ in (9) provides a transformation from a non-Gaussian vector \mathbf{y}^* to the standard Gaussian $\mathbf{z}^* = \tilde{\mathcal{T}}(\mathbf{y}^*)$; we call $\mathbf{z}^* = (z_1^*, \dots, z_N^*)$ the map coefficients corresponding to \mathbf{y}^* . Because the nonlinear dependencies have been removed, many operations are more meaningful on \mathbf{z}^* than on \mathbf{y}^* , including linear regressions, translations using linear shifts, and quantifying similarity using inner products. We can also detect inadequacies of the map $\tilde{\mathcal{T}}$ for describing the target distribution by examining the degree of non-Gaussianity and dependence in \mathbf{z}^* . These uses of transport maps will be considered further in Section 3.5.

A close relative of transport maps in machine learning are normalizing flows (see Kobayev et al., 2020, for a review), where triangular layers are used to ensure easy evaluation and inversion of likelihood objectives. Kovachki et al. (2020) also design generative adversarial networks with triangular generators that allow easy conditional sampling. Our approach can be viewed as a Bayesian autoencoder (e.g., Goodfellow et al., 2016, Ch. 14), with the posterior transport map and its inverse acting as the encoder and decoder, respectively.

2.4 Hyperparameters

The prior distributions on the f_i and d_i in Section 2.2 may depend on unknown hyperparameters $\boldsymbol{\theta}$. For example, by making inference on the σ_i in (8), we can let the data decide the degree of nonlinearity in the map and thus the non-Gaussianity in the resulting joint target distribution. We can write in closed form the integrated likelihood $p(\mathbf{Y})$, where \mathbf{f} and \mathbf{d} have been integrated out.

PROPOSITION 2. *The integrated likelihood is*

$$p(\mathbf{Y}) \propto \prod_{i=1}^N (|\mathbf{G}_i|^{-1/2} \times (\beta_i^{\alpha_i} / \tilde{\beta}_i^{\tilde{\alpha}_i}) \times \Gamma(\tilde{\alpha}_i) / \Gamma(\alpha_i)),$$

where $\Gamma(\cdot)$ denotes the gamma function, and $\tilde{\alpha}_i$, $\tilde{\beta}_i$, \mathbf{G}_i are defined in Proposition 1.

Now denote by $p_{\boldsymbol{\theta}}(\mathbf{Y})$ the integrated likelihood $p(\mathbf{Y})$ computed based on a particular value $\boldsymbol{\theta}$ of the hyperparameters. There are two main possibilities for inference on $\boldsymbol{\theta}$. First, an empirical Bayesian approach consists of estimating $\boldsymbol{\theta}$ by the value that maximizes $p_{\boldsymbol{\theta}}(\mathbf{Y})$, and then regarding $\boldsymbol{\theta}$ as fixed and known. Second, we can carry out fully Bayesian inference by specifying a prior $p(\boldsymbol{\theta})$, and sampling $\boldsymbol{\theta}$ from its posterior distribution $p(\boldsymbol{\theta}|\mathbf{Y}) \propto p_{\boldsymbol{\theta}}(\mathbf{Y})p(\boldsymbol{\theta})$ using Metropolis-Hastings; subsequent inference must then average over these posterior draws.

For all our numerical results below, we employed the empirical Bayesian approach, because it is faster and preserves the closed-form map properties in Section 2.3. In exploratory numerical experiments, we observed no significant decrease in inferential accuracy relative to the fully Bayesian approach, likely due to working with a relatively small number of hyperparameters in $\boldsymbol{\theta}$.

3 Bayesian transport maps for large spatial fields

Now assume that $\mathbf{y} = (y_1, \dots, y_N)^\top$ consists of observations $y_i = y(\mathbf{s}_i)$ of a spatial field $y(\cdot)$ at locations $\mathbf{s}_1, \dots, \mathbf{s}_N$ in a region or domain $\mathcal{D} \subset \mathbb{R}^{\dim}$. We assume Bayesian transport maps as in Section 2.1, with regressions of the form (5) in $(i-1)$ -dimensional space for $i = 1, \dots, N$. As N is very large in many relevant applications, we will specify priors distributions of the form described in Section 2.2 that induce substantial regularization and sparsity, as a function of hyperparameters $\boldsymbol{\theta}$.

3.1 Maximin ordering and nearest neighbors

A triangular map $\mathcal{T}(\mathbf{y})$ as in (1) depends on the ordering of the variables y_1, \dots, y_N . We assume that the entries of \mathbf{y} are ordered according to a maximum-minimum-distance (maximin) ordering of the corresponding locations $\mathbf{s}_1, \dots, \mathbf{s}_N$ (see Figure 2), in which we sequentially choose each location to maximize the minimum distance to all previously ordered locations. Define $c_i(k)$ as the index of the k th nearest (previously ordered) neighbor of the i th input (and so $\mathbf{s}_{c_i(1)}, \dots, \mathbf{s}_{c_i(4)}$ are indicated by $+$ in Figure 2).

The maximin ordering can be interpreted as a multiresolution decomposition into coarse scales (earlier elements of the ordering), and fine scales (later elements of the ordering). In

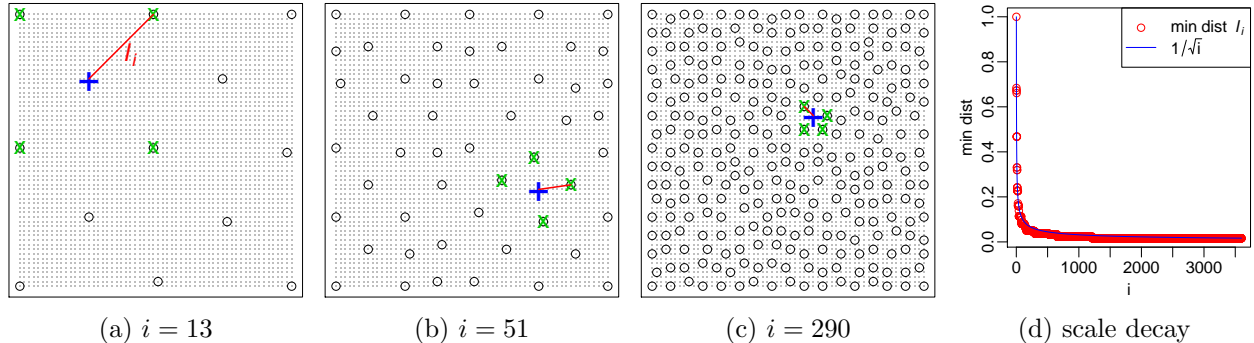


Figure 2: Maximin ordering (Section 3.1) for locations on a grid (small gray points) of size $N = 60 \times 60 = 3,600$ on a unit square, $[0, 1]^{\text{dim}}$ with $\text{dim} = 2$. (a)–(c): The i th ordered location (+), the previous $i - 1$ locations (o), including the nearest $m = 4$ neighbors (x) and the distance ℓ_i to the nearest neighbor (—). (d): For $i = 1, \dots, N$, the length scales (i.e., minimum distances) decay as $\ell_i = i^{-1/\text{dim}}$.

particular, the minimal pairwise distance $\ell_i = \|\mathbf{s}_i - \mathbf{s}_{c_i(1)}\|$ among the first i locations of the ordering decays roughly as $\ell_i \propto i^{-1/\text{dim}}$, where dim here is the dimension of the spatial domain (see Figure 2d). As a result of the maximin ordering, the i th regression in (5) can be viewed as a spatial prediction at location \mathbf{s}_i based on data at locations $\mathbf{s}_1, \dots, \mathbf{s}_{i-1}$ that lie roughly on a regular grid with distance (i.e., scale) ℓ_i .

When the variables y_1, \dots, y_N are not associated with spatial locations or when Euclidean distance between the locations is not meaningful (e.g., nonstationary, multivariate, spatio-temporal, or functional data), the maximin and neighbor ordering can be carried out based on other distance metrics, such as $(1 - |\text{correlation}|)^{1/2}$ based on some guess or estimate of the correlation between variables (Kidd and Katzfuss, 2021). An example of this idea can be found in Section 6.

3.2 Priors on the conditional non-Gaussianity σ_i^2

In (8), σ_i^2 determines the degree of nonlinearity in \mathcal{T}_i ; hence, $\sigma_i^2, \dots, \sigma_N^2$ together determine the conditional non-Gaussianity in the distribution of $\mathbf{y}_{i:N}$ given $\mathbf{y}_{1:i-1}$. A priori, we assume that the degree of nonlinearity decays polynomially with ℓ_i , namely $\sigma_i^2 = e^{\theta_{\sigma,1}} \ell_i^{\theta_{\sigma,2}}$, which allows the conditional distributions of $\mathbf{y}_{i:N}$ given $\mathbf{y}_{1:i-1}$ to be increasingly Gaussian as i increases, as a function of hyperparameters $\theta_{\sigma,1}, \theta_{\sigma,2}$.

This prior assumption is motivated by the behavior of stochastic processes with quasiquadratic loglikelihoods. A quasiquadratic loglikelihood of order r is the sum of a quadratic leading-order term that depends on the r -th derivatives of the process, and a nonquadratic term that may only depend on derivatives up to order $r - 1$. Gaussian smoothness priors (with quadratic loglikelihoods) such as the Matérn model (Whittle, 1954, 1963) are closely related to linear partial differential equations (PDEs); similarly, stochastic processes with quasiquadratic loglikelihood are closely related to quasilinear PDEs, where terms involving the highest-order derivatives are required to be linear. A wide range of physical phenomena is governed by quasilinear PDEs. For instance, the Cahn-Hilliard (Cahn and Hilliard, 1958) and Allen-Cahn (Allen and Cahn, 1972) equations describe phase separation in multi-component systems, the Navier-Stokes equation describes the dynamics of fluids, and the

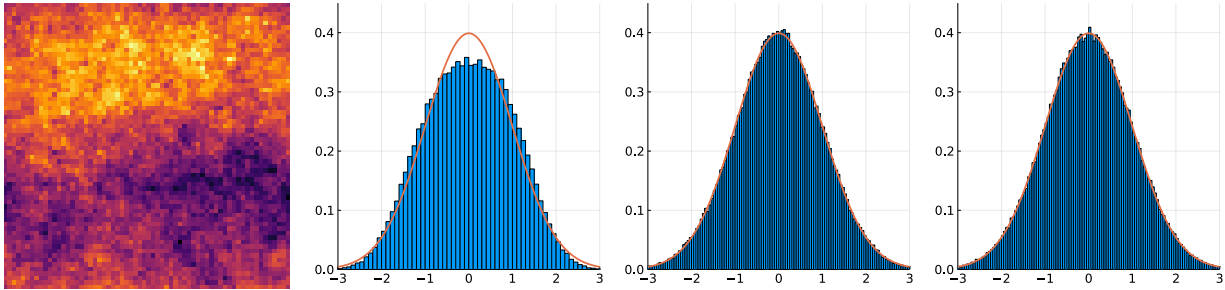


Figure 3: Samples from the non-Gaussian process given by (21) feature regions of negative (dark) and positive (light) values (first panel). The distribution values at any given site is a mixture between those two possibilities and thus non-Gaussian (second panel). By contrast, after conditioning on averages over regions of size $\ell = 2^{-1}$ (third panel) or $\ell = 2^{-5}$ (fourth panel), the conditional distribution is close to Gaussian, as these averages determine with high probability whether a given site is in a positive or negative region.

Föppl-von Kármán equations describe the large deformations of thin elastic plates.

By using Poincaré inequalities (Adams and Fournier, 2003) one can show, roughly speaking, that conditional on measurements on a length scale ℓ , the q -th derivatives of a perturbation to the stochastic process have magnitude $\approx \ell^q$. Thus, the linear leading-order term becomes the dominant contribution to the loglikelihood on smaller scales and, accordingly, the conditional distribution is approximately Gaussian. This is illustrated in a numerical example in Figure 3. A more detailed description of these results and the illustration in Figure 3 is provided in Appendix B.

3.3 Priors on the conditional variances d_i^2

As we have argued in Section 3.2, even non-Gaussian stochastic processes with quasi-linear log-likelihoods exhibit conditional near-Gaussianity on fine scales. Thus, we will now describe prior assumptions for the d_i^2 and f_i in (5) that are motivated by the behavior of a transport map \mathcal{T} for a Gaussian target distribution. Specifically, our priors are motivated by a Gaussian distribution with Matérn covariance (see Figure 4), which is a highly popular assumption in spatial statistics. The Matérn covariance function is also the Green’s function of an elliptic PDE (Whittle, 1954, 1963).

Schäfer et al. (2021b, Thm. 2.3) show that Gaussian processes with covariance functions given by the Green’s function of elliptic PDEs of order r have conditional variance of the order ℓ_i^{2r} when conditioned on the first i elements of the maximin ordering, where ℓ_i are the length scales in the maximin ordering (see Figure 4b).

Hence, for the noise or conditional variances $d_i^2 \sim \mathcal{IG}(\alpha_i, \beta_i)$ as in Section 2.2, we set $E(d_i^2) = \beta_i/(\alpha_i - 1) = e^{\theta_{d,1}} \ell_i^{\theta_{d,2}}$. Assuming the prior standard deviation of d_i^2 to be equal to g times the mean, we obtain $\alpha_i = 2 + 1/g^2$ and $\beta_i = e^{\theta_1} \ell_i^{\theta_2} (1 + 1/g^2)$. For our numerical experiments, we arbitrarily chose $g = 4$ to obtain a relatively vague prior for the d_i^2 .

3.4 Priors on the regression functions f_i

The regression functions $f_i : \mathbb{R}^{i-1} \rightarrow 1$ in (5) were specified to be GPs in $(i - 1)$ -dimensional space in Section 2.2. For the covariance function in (8), we assume that $\rho_i(\mathbf{y}_{1:i-1}, \mathbf{y}'_{1:i-1}) =$

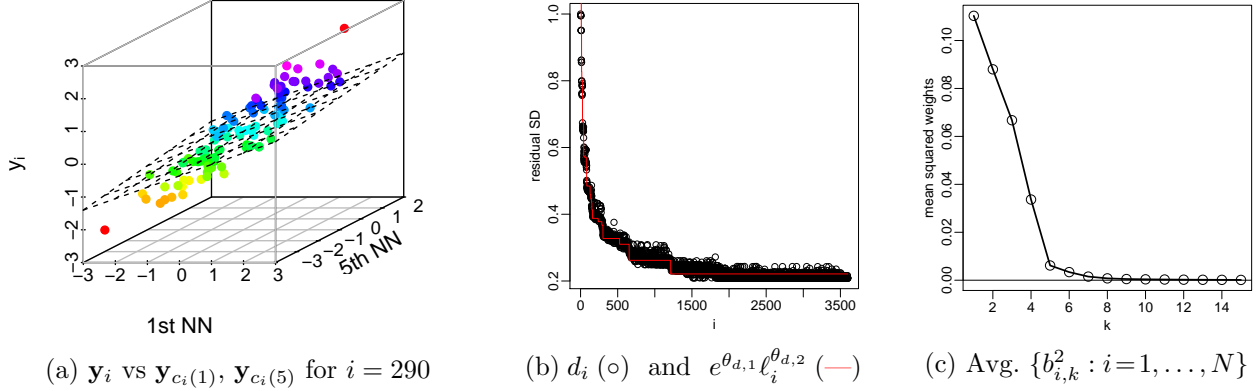


Figure 4: For a *Gaussian* process with exponential covariance on the grid and with the ordering from Figure 2, expressing the joint distribution $p(\mathbf{y})$ using a transport map as in (1)–(3) results in a series of regressions as in (5) with *linear* predictors, $f_i(\mathbf{y}_{1:i-1}^{(j)}) = \sum_{k=1}^{i-1} y_{c_i(k)}^{(j)} b_{i,k}$, where $c_i(k)$ indicates the k th nearest (previously ordered) neighbor of the i th input. (For non-Gaussian $p(\mathbf{y})$, the functions f_i are *nonlinear*.) (a): For $n = 100$ simulations, the values of \mathbf{y}_i and its 1st and 5th nearest neighbor (NN) lie on a low-dimensional manifold; the regression plane (assuming all other variables to be fixed) indicates a stronger influence of the 1st NN (see the slope of the intersection of the regression plane with the front of the box) than of the 5th NN. (b): The conditional standard deviations decay as a function of the length scale ℓ_i (see Figure 2d). (c) The squared regression coefficients decay rapidly as a function of neighbor number k .

$\rho(\mathbf{y}_{1:i-1}^\top \mathbf{Q}_i \mathbf{y}'_{1:i-1} / \gamma)$, where $\gamma = \exp(\theta_\gamma)$ is a range parameter and ρ is an isotropic correlation function, taken to be Matérn with smoothness 1.5 for all numerical experiments here.

To make this potentially high-dimensional regression feasible, we again use the example of a spatial GP with Matérn covariance to motivate regularization and sparsity via the relevance matrix $\mathbf{Q}_i = \text{diag}(q_{i,1}^2, \dots, q_{i,i-1}^2)$. We assume that the relevance of the k th neighbor (see Section 3.1) decays exponentially as a function of k , such that $q_{i,c_i(k)}$ decays as $\exp(\theta_q k)$. This type of behavior, often referred to as screening effect (e.g., Stein, 2011), is illustrated in Figure 4c, and it has been exploited for covariance estimation of a Gaussian spatial field by Kidd and Katzfuss (2021). Recently, Schäfer et al. (2021b) proved exponential rates of screening for Gaussian processes derived from elliptic boundary-value problems; following the discussion in Section 3.2, we expect similar conditional independence phenomena to hold on the fine scales of processes with quasiquadratic loglikelihoods.

Given this exponential decay as a function of the neighbor number k , the relevance will be essentially zero for sufficiently large k , and so we achieve sparsity by setting

$$q_{i,c_i(k)} = \begin{cases} \exp(\theta_q k), & k \leq m, \\ 0, & k > m, \end{cases} \quad (14)$$

where the sparsity parameter $m = \max\{k : \exp(\theta_q k) \geq \varepsilon\}$ is determined by the data through the hyperparameter θ_q . We use $\varepsilon = 0.01$ for our numerical examples. This assumption induces a sparse transport map, in that f_i (and thus \mathcal{T}_i) depend on $\mathbf{y}_{1:i-1}$ only through $y_{c_i(1)}, \dots, y_{c_i(m)}$, where ρ_i is isotropic as a function of the scaled inputs $y_{c_i(k)} / q_{i,c_i(k)}$. Sparsity in the transport map is equivalent to an assumption of ordered conditional independence (cf. Spantini et al., 2018), which can be seen from the expression of the conditional distributions in (4). Similar ordered-conditional-independence assumptions are also popular for fast

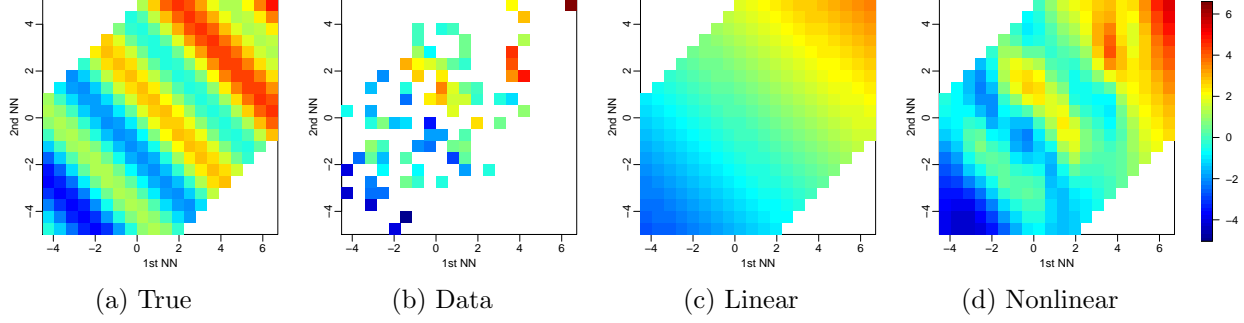


Figure 5: Simulation from a nonlinear map with sine structure in f_i , described as NR900 in Section 5. For $n = 100$ and $i = 80$, y_i versus its 1st and 2nd nearest neighbor (NN): true f_i (a), observations \mathbf{y}_i (b), together with linear (c) and nonlinear (d) fit (i.e., posterior means) of f_i , with further variables in $\mathbf{y}_{1:i-1}$ held at their mean levels. The linear map in (c) is estimated under the restriction $\sigma_i = 0$. In (d), we have a nonlinear regression in 79-dimensional space, with $m = 5$ active variables in the estimated (via $\boldsymbol{\theta}$) nonlinear model.

approximations of Gaussian fields with parametric covariance functions (e.g., Vecchia, 1988; Stein et al., 2004; Datta et al., 2016; Guinness, 2018; Katzfuss and Guinness, 2021; Katzfuss et al., 2020a,b; Schäfer et al., 2021a).

Identifying the regression functions f_i in m -dimensional space is further aided by the data concentrating on a lower-dimensional manifold due to the strong dependence between most $y_{c_i(k)}$ and $y_{c_i(l)}$ for small $k, l \leq m$ (e.g., see Figure 4a).

3.5 Inference

Based on the prior distributions in Sections 3.2–3.4, we can carry out inference and compute the transport map as in Section 2.3. Due to the sparsity assumption in (14), the computational complexity is lower than in Section 2.3; specifically, determining $\tilde{\mathcal{T}}_i$ now only requires $\mathcal{O}(n^3 + mn^2)$ time, again in parallel for each $i = 1, \dots, N$. Each application of the transport map or its inverse then requires $\mathcal{O}(N(n^2 + mn))$ time. The maximin ordering and nearest neighbors can also be computed in quasilinear time in N (Schäfer et al., 2021a, Alg. 7).

The prior distributions in Sections 3.2–3.4 depend on a vector of hyperparameters, $\boldsymbol{\theta} = (\theta_{\sigma,1}, \theta_{\sigma,2}, \theta_{d,1}, \theta_{d,2}, \theta_\gamma, \theta_q)$. When making inference on $\boldsymbol{\theta}$ as described in Section 2.4, we effectively let the training data \mathbf{Y} decide the degree of sparsity (through θ_q via m) and the degree of nonlinearity (through $\theta_{\sigma,1}, \theta_{\sigma,2}$ via σ_i).

Figure 5 illustrates estimation of transport-map components in a simulated example.

In Section 2.3, we discussed using $\tilde{\mathcal{T}}$ in (9) to transform the non-Gaussian data \mathbf{y}^* to standard Gaussian map coefficients $\mathbf{z}^* = \tilde{\mathcal{T}}(\mathbf{y}^*)$. This concept, which is illustrated in Figure 6, is especially interesting in our spatial setting. Due to the maximin ordering (Figure 2), the scales ℓ_i are arranged in decreasing order, and in our prior the d_i^2 also follow a decreasing stochastic order with $E(d_i^2) = e^{\theta_{d,1}} \ell_i^{\theta_{d,2}}$ (see, e.g., Figure 4b). Thus, we can view the map components as a form of nonlinear principal components (NPCs), with the map coefficients as the corresponding component scores. For Gaussian processes with covariance functions given by the Green’s function of elliptic PDEs, similar to the Matérn family, it can be shown that these principal components based on the maximin ordering are approximately optimal (Schäfer et al., 2021b). For example, these NPCs can be used for dimension reduction by

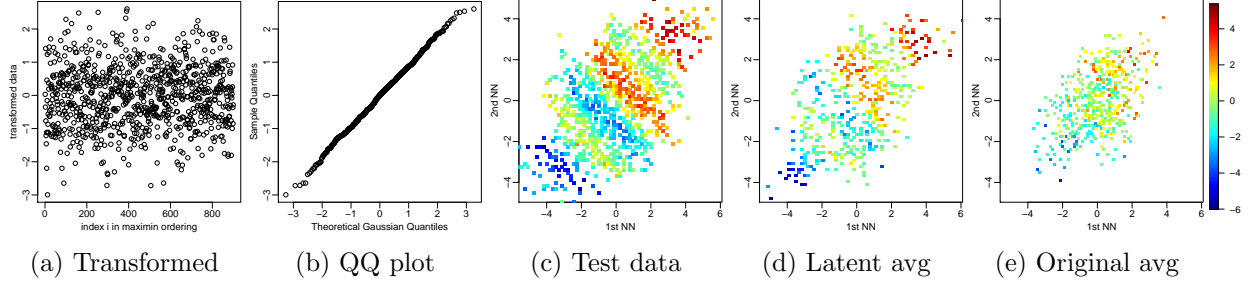


Figure 6: Illustration of map coefficients \mathbf{z}^* (see Sections 2.3 and 3.5) for the simulated NR900 data using a map (9) inferred from $n = 100$ training data. (a)–(b): The $N = 900$ map coefficients corresponding to one test sample are roughly iid Gaussian. (c): For 1,000 test samples, y_{80}^* versus 1st and 2nd NNs (cf. Figure 5). (d) When averaging two map coefficients at a time in latent space and transforming back to the original space using (12), the nonlinear (sinusoidal) relationship between y_{80}^* and its NNs is preserved in the resulting 500 averages. (e) When averaging the test samples directly in original space, the nonlinear structure is lost.

only storing or modeling the first k , say, map coefficients $\mathbf{z}_{1:k}^* = (z_1^*, \dots, z_k^*)^\top$. Note that if we set $\mathbf{z}_{k+1:n}^* = \mathbf{0}$, we assume $y_i^* = \hat{f}_i(\mathbf{y}_{1:i-1}^*)$ for $i > k$, which overestimates dependence and underestimates variability; hence, instead, we should always draw $\mathbf{z}_{k+1:n}^* \sim \mathcal{N}(\mathbf{0}, \mathbf{I})$. In addition to reducing storage, we can also use this approach for conditional simulation (Marzouk et al., 2016, Lemma 1), in which we fix the large-scale features of an observed field by fixing the first k map coefficients (see Figure 10 for an illustration). To model a time series of spatial fields, we can for example assume a linear vector autoregressive model for the NPCs, such that the map coefficients at time $t + 1$, say $\mathbf{z}_{1:k}^{(t+1)}$, linearly depend on $\mathbf{z}_{1:k}^{(t)}$. When it is of interest to regress some response on a spatial field, one could also use the first k map coefficients of the field as the covariates, similar to the use of function principal component scores in regression.

4 Marginal non-Gaussianity

So far, we have focused on nonlinear, non-Gaussian dependence structures; the model described in Sections 2 and 3 is most appropriate if the marginal distribution of each y_i is Gaussian. If this does not hold at least approximately, extensions based on additional marginal (i.e., pointwise) transformations are straightforward. For example, assume that the model from Sections 2 and 3 holds for \mathbf{y} , but that we actually observe $\tilde{\mathbf{y}} = \mathcal{G}(\mathbf{y})$ such that $\tilde{y}_i = g_i(y_i)$. If the g_i are one-to-one differentiable functions, the resulting posterior map is a simple extension of that in Proposition 1. The g_i can be pre-determined (see Section 6 for an example with a log transform) or may depend on $\boldsymbol{\theta}$ and thus be inferred based on a minor modification of the integrated likelihood in Proposition 2.

For marginal distributions that are continuous but are not easily transformed to Gaussianity, we will extend our GP regressions with Gaussian error (see (5)) to modeling the GP errors $\epsilon_i^{(j)}$ using Bayesian nonparametrics for all $i = 1, \dots, N$. More precisely, we will use Dirichlet process mixtures (DPM) with Gaussian base measures. In (5), we now assume that $f_i(\cdot) \sim \mathcal{GP}(0, C_i)$, and the $\epsilon_i^{(j)}$ are distributed according to a DPM:

$$\epsilon_i^{(j)} | \mu_i, d_i \sim \mathcal{N}(\mu_i, d_i^2), \quad (\mu_i, d_i^2) | \mathcal{F}_i \sim \mathcal{F}_i, \quad \mathcal{F}_i \sim \mathcal{DP}(\mathcal{NIG}(\xi_i, \eta_i, \alpha_i, \beta_i), \zeta_i),$$

where ζ_i is the concentration parameter, and the base measure \mathcal{NIG} is a normal-inverse-Gamma distribution with parameters $\xi_i, \eta_i, \alpha_i, \beta_i$ with $\xi_i = 0$. The degree of non-Gaussianity allowed for the $\epsilon_i^{(j)}$ is determined by η_i and ζ_i ; a small value of ζ_i concentrates the Dirichlet process near the NIG base measure, for which a large value of η_i shrinks μ_i toward zero. Thus, in the limit as $\zeta_i \rightarrow 0$ and $\eta_i \rightarrow \infty$, we obtain a model similar to that in Section 2.2 (except that here d_i^2 does not appear in the variance of the GP f_i).

For the spatial setting with maximin ordering of Section 3, we can again find a sparse parameterization in terms of hyperparameters $\boldsymbol{\theta} = (\theta_{\sigma,1}, \theta_{\sigma,2}, \theta_{d,1}, \theta_{d,2}, \theta_\gamma, \theta_q, \theta_{\zeta,1}, \theta_{\zeta,2}, \theta_{\eta,1}, \theta_{\eta,2})$. We parameterize the α_i, β_i, C_i in terms of $\theta_{\sigma,1}, \theta_{\sigma,2}, \theta_{d,1}, \theta_{d,2}, \theta_\gamma, \theta_q$ as in Sections 3.2–3.4. For the concentration parameter $\zeta_i = e^{\theta_{\zeta,1}} \ell_i^{\theta_{\zeta,2}}$, we allow increasing shrinkage towards Gaussianity for increasing i . We similarly set $\eta_i = e^{\theta_{\eta,1}} \ell_i^{\theta_{\eta,2}}$. For this DPM model, we take a fully Bayesian perspective and assume a flat, improper uniform prior for $\boldsymbol{\theta}$ over \mathbb{R}^{10} .

Due to the nonparametric nature of the DPM and the GP assumptions with nonzero prior probability for the dense (non-sparse) transport map, the posterior distribution obtained using this model contracts (for $n \rightarrow \infty$ and fixed N) to the KL projection of the actual distribution of \mathbf{y} onto the space of distributions that can be described by a transport map whose components are additive in the i th argument as in (3), due to the KL optimality of the Knothe-Rosenblatt map (Marzouk et al., 2016, Sec. 4.1). In other words, as the number of replicates increases, the learned distribution gets as close as possible to the truth under the additivity restriction.

Inference for our DPM model cannot be carried out in closed form anymore, and instead relies on a Metropolis-within-Gibbs Markov chain Monte Carlo (MCMC) sampler. We can also compute and draw samples from the posterior predictive distribution

$$p(\mathbf{y}^*|\mathbf{Y}) = \prod_{i=1}^N p(y_i^*|\mathbf{y}_{1:i-1}^*, \mathbf{Y}),$$

for which each $p(y_i^*|\mathbf{y}_{1:i-1}^*, \mathbf{Y})$ is approximated as a Gaussian mixture based on the MCMC output. Details for the MCMC procedure and the posterior predictive distribution are given in Appendix C.

In the spatial setting with sparsity parameter m , each MCMC iteration still has time complexity $\mathcal{O}(N(n^3 + n^2m))$ and the computations within each iteration are highly parallel; however, the actual computational cost for this sampler is much higher than in Section 3.5 due to the typically large number of MCMC iterations required.

5 Simulation study

We carried out a simulation study based on true maps as in Section 2.1, with the f_i and d_i as implied by extensions of a Gaussian process (GP) with exponential covariance evaluated at locations on a unit square. Specifically, we considered the following four simulation scenarios:

LR900: Linear map (i.e., a Gaussian distribution) with components f_i^L based on an exponential covariance with unit variance and range parameter 0.3 evaluated on a **Regular** grid of size $N = 30 \times 30 = \mathbf{900}$.

NR900: Nonlinear extension of LR900 by a sine function of a weighted sum of the nearest two neighbors, with $f_i^{\text{NL}}(\mathbf{y}_{1:i-1}) = f_i^L(\mathbf{y}_{1:i-1}) + 2 \sin(4(y_{i,c_i(1)} + y_{i,c_i(2)}))$ (see Figure 5a)

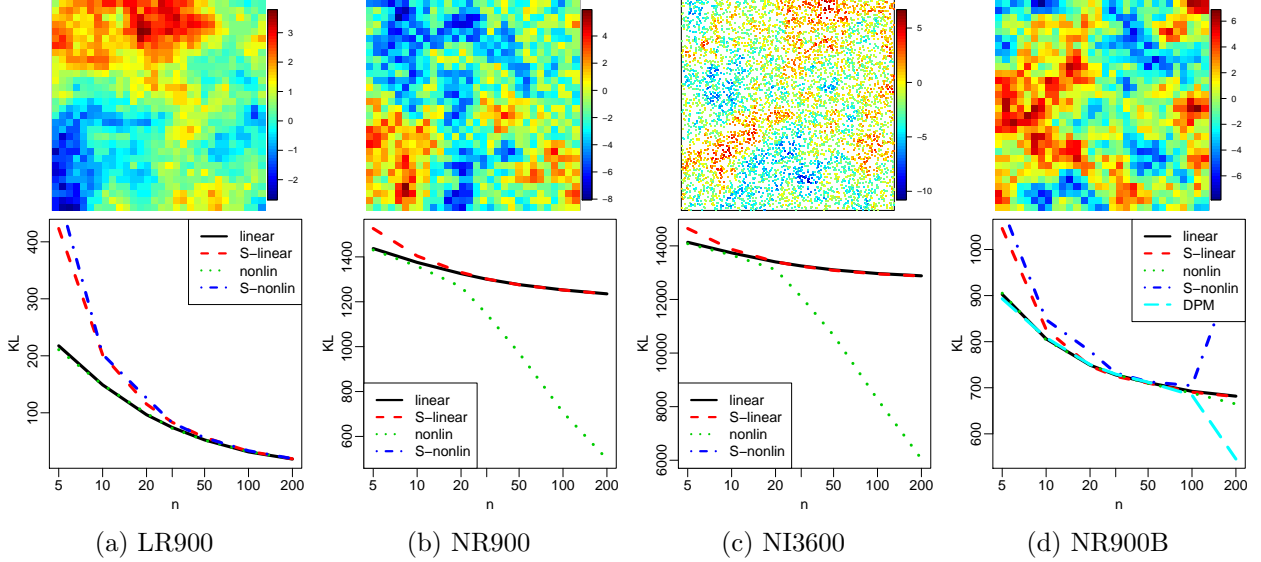


Figure 7: Top row: Simulated spatial fields for four simulation scenarios described in Section 5. Bottom row: Corresponding comparisons of KL divergence as a function of ensemble size n (on a log scale) for different methods. In (b)–(c), the KL divergence for **S-nonlin** was extremely high and thus is not shown. **DPM** is only included in (d).

NI3600: Same as NR900, but based on an exponential covariance at $N = 3,600$ Irregularly spaced locations sampled uniformly at random

NR900B: Same as NR900, but with a **Bimodal** distribution for the ϵ_i in (5): $\epsilon_i | \mu_i \sim \mathcal{N}(\mu_i, d_i^2)$ with μ_i sampled from $\{-3.5d_i, 3.5d_i\}$ with equal probability

For computational simplicity, each (true) f_i was assumed to only depend on the nearest 30 previously ordered neighbors, but this gives a highly accurate approximation of a “full” exponential covariance in the linear MR900 case. Samples from LR900, NR900, and NR900B are illustrated in the top row of Figure 7.

We compared the following methods:

nonlin: Our method with Bayesian uncertainty quantification, as described in Section 3

S-nonlin: Simplified version of **nonlin** ignoring uncertainty in the f_i and d_i , as in (13)

linear: Same as **nonlin**, but forcing $\theta_{\sigma,1} = -\infty$ and hence linear f_i

S-linear: Simplified version of **linear** ignoring uncertainty in the f_i and d_i , as in (13)

DPM: The model with Dirichlet process mixture residuals in Section 4

We carried out fully Bayesian inference for **DPM** using the MCMC procedure in Appendix C; for all other methods, we carried out empirical Bayesian inference based on a plug-in estimate of the hyperparameters θ as described at the end of Section 2.4. Note that **S-linear** is the only method that results in a joint Gaussian posterior predictive distribution; **S-linear** is similar to the approach proposed and used in numerical comparisons in Kidd and Katzfuss (2021).

Some properties of our nonlinear approach are illustrated in Figures 5 and 6. Our nonlinear method estimated f_i well in the observed high-probability region.

Figure 7 shows the results of more systematic comparisons using the Kullback-Leibler

(KL) divergence,

$$E(\log p_0(\mathbf{y})) - E(\log p(\mathbf{y}|\mathbf{Y})) \quad (15)$$

between the true distribution $p_0(\mathbf{y})$ and the distribution $p(\mathbf{y}|\mathbf{Y})$ implied by the inferred posterior map (see (18)), where the expectations are taken with respect to the true distribution. We approximated the expectations by the sample means over 50 simulated test fields \mathbf{y}^* , and so the resulting KL divergence is the difference of the log-scores (e.g. Gneiting and Katzfuss, 2014) of the true and inferred distributions. Whenever nonlinear structure was not discernible from the data (because the true map was linear or because the ensemble size n was too small), `nonlin` performed similarly to `linear` and hence did not suffer due to its overflexibility. For larger ensemble size and nonlinear truths, `nonlin` at times far outperformed `linear`. `S-linear` and `S-nonlin` were generally less accurate than their counterparts with uncertainty quantification; in the linear case, this was only an issue for small ensemble size; `S-nonlin` performed extremely poorly when the nonlinear structure was clearly apparent in the data, likely due to overfitting without accounting for uncertainty in the fit.

6 Climate-data application

An important application of our methods is the analysis and emulation of output from climate models. Climate models are essentially large sets of computer code describing the behavior of the Earth system (e.g., the atmosphere) via systems of differential equations. Much time and resources have been spent on developing these models, and enormous computational power is required to produce ensembles (i.e., solve the differential equations for different starting conditions) on fine latitude-longitude grids for various scenarios of greenhouse-gas emissions. Of the large amount of data and output that have been generated, only a small fraction has been fully explored or analyzed (e.g. Benestad et al., 2017). A popular way of analyzing climate-model output is statistical emulation (e.g., Castruccio and Stein, 2013; Castruccio et al., 2014; Nychka et al., 2018), which aims to infer the distribution of one or more climate variables, so that relevant summaries or additional samples can be computed more cheaply than via more runs of the full climate model.

We considered log-transformed total precipitation rate (in m/s) on a roughly 1° longitude-latitude global grid of size $N = 288 \times 192 = 55,296$ on July 1 in 98 consecutive years, starting in the year 402, from the Community Earth System Model (CESM) Large Ensemble Project (Kay et al., 2015). We obtained precipitation anomalies by standardizing the data at each grid location to mean zero and variance one, shown in Figure 1

For ease of comparison and illustration, we first considered a smaller of size $N = 37 \times 74 = 2,738$ in a subregion containing large parts of the Americas (45°S to 45°N and 130°W to 30°W). The anomalies in this subregion also exhibited a nonstationary dependence structure due to ocean, land, and mountains. Hence, we used the correlation-based ordering discussed in Section 3.1, based on a correlation-matrix estimate given by the element-wise product between the sample covariance and an exponential covariance with a large range parameter. As shown in Figure 8a, the precipitation anomalies exhibited similar features as our simulated data in Figure 4a, with regression data concentrating on lower-dimensional manifolds.

For comparing the methods from Section 5 on the precipitation anomalies, computing the KL divergence as in (15) was not possible, as the true distribution $p_0(\mathbf{y})$ was unknown. Hence,

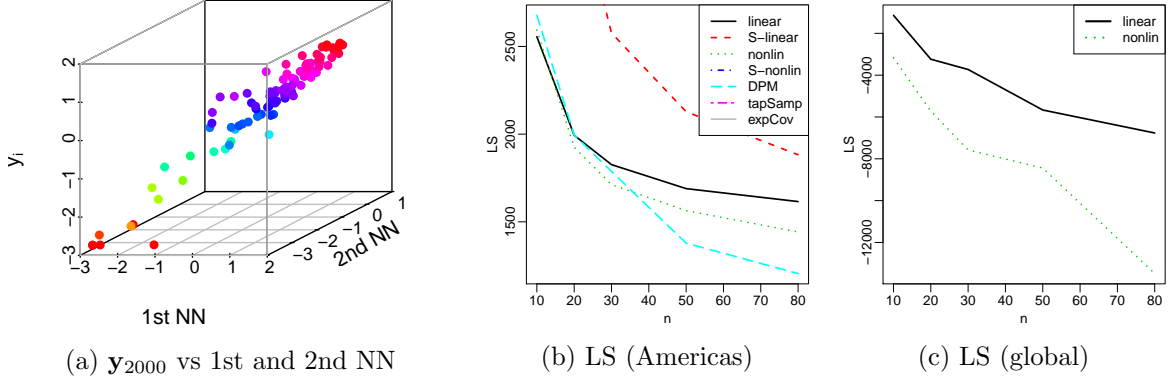


Figure 8: For precipitation anomalies: (a) Our approach can be viewed as N regressions, of each y_i on ordered nearest neighbors (NNs), as in Figure 4, with the regression data on low-dimensional manifolds. (b) Comparison of log-score (LS; equal to KL divergence up to an additive constant) for estimated joint distribution for the Americas subregion as a function of ensemble size n ; the LS for **S-linear**, **tapSamp**, and **expCov** were too high (all $> 20,000$) and are thus not visible. (c) LS for **linear** and **nonlin** for precipitation anomalies on the global grid.

we compared the methods using various training data sizes n in terms of log-scores, which are approximately equal to the KL divergence up to an additive constant; specifically, these log-scores consist of the second part of (15), $-E(\log p(\mathbf{y}|\mathbf{Y}))$, approximated by averaging over 18 test replicates and over five random training/test splits. The comparison for the Americas subregion is shown in Figure 8b; **nonlin** outperformed **linear**, and DPM was even more accurate than **nonlin** for large n , indicating that the precipitation anomalies exhibited joint and marginal non-Gaussian features. As in Section 5, **S-linear** and **S-nonlin** performed poorly due to ignoring uncertainty in the estimated map. We also compared to two baseline competitors that combine a (zero-mean) multivariate-Gaussian assumption with different covariance-matrix estimates: the sample covariance tapered (i.e., element-wise multiplied) by an exponential correlation matrix with range equal to the maximum pairwise distance among the locations (**sampTap**), and an exponential covariance with variance and range estimated from the training data (**expCov**); both baseline competitors performed poorly.

We also considered the map coefficients $\mathbf{z}^* = \tilde{\mathcal{T}}(\mathbf{y}^*)$ discussed in Sections 2.3 and 3.5, using the map obtained by fitting **nonlinear** to the first $n = 97$ replicates as training data. In Figure 9a, the map coefficients for a held-out test field appeared roughly iid standard Gaussian, with the sample autocorrelations near zero (not shown). Figure 9 also illustrates that the map coefficients offer similar properties for non-Gaussian fields as principal-component scores do for Gaussian settings. For example, the medians of the posterior distributions of the d_i (see (17)) decreased rapidly as a function of i , which means that the map coefficients early in the maximin ordering captured much more (nonlinear) variation than later-ordered coefficients (see, e.g., (12) and (13)). Further, we computed the map coefficients for all 98 replicates for July 2–30, and the lag-1 autocorrelation over time between map coefficients also decreased with i . Specifically, while most of the first 100 were greater than 0.2, many later autocorrelations were negligible; this indicates that a spatio-temporal analysis could proceed by fitting a simple (linear) autoregressive model over time to only the first k , say, map coefficients, while treating the remaining $n - k$ map coefficients as independent over

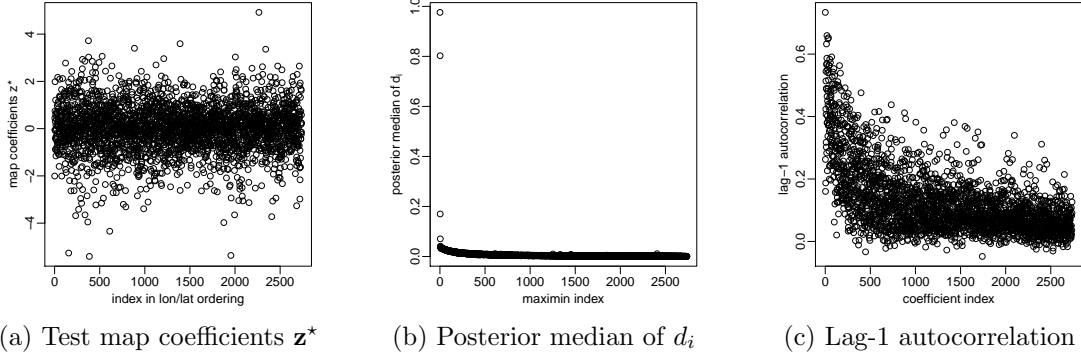


Figure 9: Properties of the map coefficients $\mathbf{z}^* = \tilde{\mathcal{T}}(\mathbf{y}^*)$ for the precipitation anomalies on the grid of size $N = 2,738$ in the Americas subregion. (a): The map coefficients corresponding to the test field in Figure 10a in the original data ordering (first by longitude, then latitude) appeared roughly iid standard Gaussian, aside from slightly heavy tails. (b): The posterior medians of the d_i decreased rapidly as a function of i , meaning that the first few map coefficients captured much more variation than later-ordered coefficients. (c): The autocorrelation between consecutive days also decreased with i ; while most of the first 100 were greater than 0.2, many later autocorrelations were negligible.

time.

To demonstrate scalability to large datasets, we applied and compared **linear** and **nonlinear** on the entire global precipitation anomaly fields of size $N = 288 \times 192 = 55,296$. We used a maximin ordering based on chordal distance. As shown in Figure 8c, **nonlin** outperformed **linear** even more decisively than for the smaller spatial region. Even in the largest and most accurate setting ($n = 80$), the estimated $\boldsymbol{\theta}$ for **nonlinear** implied $m = 9$, meaning that the corresponding transport map was extremely sparse and hence computationally efficient. Also, all but 113 of the $N = 55,296$ posterior medians of the d_i were more than 20 times smaller than the largest posterior median (i.e., that of d_1), indicating that our approach could be used for massive dimension reduction without losing too much information.

Finally, the fitted map (or rather, its inverse $\tilde{\mathcal{T}}^{-1}$) can also be viewed as a stochastic emulator of the climate model. Specifically, we can produce a new precipitation-anomaly sample by drawing $\mathbf{z}^* \sim \mathcal{N}_N(\mathbf{0}, \mathbf{I}_N)$ and then computing $\mathbf{y}^* = \tilde{\mathcal{T}}^{-1}(\mathbf{z}^*)$. One such sample (for the full global grid) is shown in Figure 10d; it can be generated in a few seconds on a basic desktop computer. Further, this approach can also be used to draw conditional samples, in which we fix the first i , say, map coefficients, for example at the values corresponding to a given spatial field. Such draws, which maintain the large-scale features in the held-out (98th) test field but allow for newly sampled fine-scale features, are shown in Figure 10. This is related to the supervised conditional sampling ideas in Kovachki et al. (2020), with their inputs given by our first i ordered test observations.

7 Conclusions

We have developed a Bayesian approach to inferring a non-Gaussian target distribution via a transport map from the target to a standard normal distribution. The components of the map are modeled using Gaussian processes. For the distribution of spatial fields, we

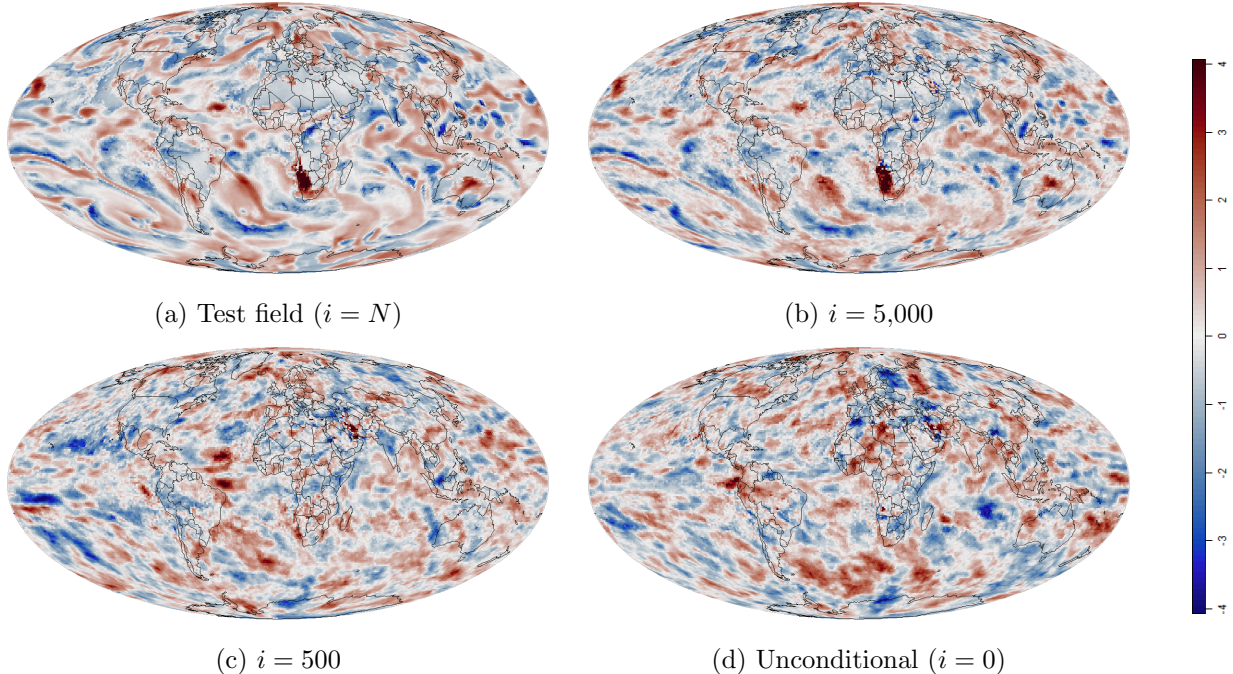


Figure 10: For the global climate data ($N = 55,296$), we fitted a stochastic emulator using `nonlin` based on $n = 97$ training replicates. Given a held-out test field \mathbf{y}^* in (a), we show conditional simulations based on fixing the first i map coefficients in $\mathbf{z}^* = \tilde{\mathcal{T}}(\mathbf{y}^*)$. (b): Only differs in some fine-scale features from (a). (c): Some large-scale features from (a) are preserved. (d): Unconditional simulation (i.e., independent from (a)).

have developed specific prior assumptions that result in sparse maps and thus scalability to high dimensions. Instead of manually or iteratively expanding a finite-dimensional parameterization of the transport map (e.g., El Moselhy and Marzouk, 2012; Bigoni et al., 2016; Marzouk et al., 2016), our Bayesian approach probabilistically regularizes the map; the resulting approach is flexible and nonparametric, but guards against overfitting and quantifies uncertainty in the estimation of the map. In our numerical comparisons, this accounting for uncertainty led to vastly improved accuracy, and the flexibility did not reduce the accuracy even when the true distribution was Gaussian. Due to conjugate priors and the resulting closed-form expressions for the posterior map and its inverse, our approach also allows us to convert non-Gaussian data into iid normal map coefficients, which can be thought of as a nonlinear extension of principal components.

As our approach essentially turns estimation of a high-dimensional joint distribution into a series of GP regressions, it is straightforward to include additional covariates and examine their nonlinear, non-Gaussian effect on the distribution. Shrinkage toward a joint Gaussian distribution with a parametric covariance function could be achieved by assuming the mean for the GP regressions to be the one implied by a Vecchia approximation of that covariance function (Kidd and Katzfuss, 2021). Extensions to more complicated input domains (e.g., space-time) could be obtained using correlation-based ordering (Section 3.1). More generally, one could envision an iterative procedure: find an initial estimate of the dependence structure, carry out our transport-map procedure based on the resulting correlation-based ordering, and then use the dependence implied by the resulting map to reorder, and so on.

Finally, another major avenue of future work would be to use the inferred distribution as the prior of a latent field, which we then update to obtain a posterior given noisy observations of the field; among countless other applications, this would enable the use of our technique to infer the forecast distribution and account for uncertainty in ensemble-based data assimilation (Boyles and Katzfuss, 2021), leading to nonlinear updates for non-Gaussian applications.

Acknowledgments

Katzfuss was partially supported by National Science Foundation (NSF) Grants DMS-1654083, DMS-1953005, and CCF-1934904. Schaefer gratefully acknowledges support by the Air Force Office of Scientific Research under award number FA9550-18-1-0271 (Games for Computation and Learning), and the Office of Naval Research under award N00014-18-1-2363 (Toward scalable universal solvers for linear systems). We would like to thank Joe Guinness for helpful comments and discussions.

A Proofs

Proof of Proposition 1. Combining (4) with the conditional independence of $\mathbf{y}^{(1)}, \dots, \mathbf{y}^{(n)}$, we have

$$p(\mathbf{Y}|\mathbf{F}, \mathbf{d}) = \prod_{i=1}^N \prod_{j=1}^n \mathcal{N}(y_i^{(j)} | f_i(\mathbf{y}_{1:i-1}^{(j)}), d_i^2) = \prod_{i=1}^N \mathcal{N}(\mathbf{y}_i | \mathbf{f}_i, d_i^2 \mathbf{I}_n), \quad (16)$$

where $\mathbf{F} = (\mathbf{f}_1, \dots, \mathbf{f}_N)$, and $\mathbf{f}_i = f_i(\mathbf{Y}_{1:i-1}) = (f_i(\mathbf{y}_{1:i-1}^{(1)}), \dots, f_i(\mathbf{y}_{1:i-1}^{(n)}))^\top$ is distributed as $\mathbf{f}_i | d_i, \mathbf{Y}_{1:i-1} \sim \mathcal{N}(\mathbf{0}, d_i^2 \mathbf{K}_i)$, with $\mathbf{K}_i = K_i(\mathbf{Y}_{1:i-1}, \mathbf{Y}_{1:i-1}) = (K_i(\mathbf{y}_{1:i-1}^{(j)}, \mathbf{y}_{1:i-1}^{(l)}))_{j,l=1,\dots,n}$. Combined with (6), we see that \mathbf{f}_i, d_i (conditional on $\mathbf{Y}_{1:i-1}$) jointly follow a (multivariate) normal-inverse-gamma (NIG) distribution, independently for each \mathbf{f}_i, d_i . Given the data \mathbf{Y} as in (16), well-known conjugacy results imply that the posterior also consists of independent NIG distributions:

$$p(\mathbf{F}, \mathbf{d}|\mathbf{Y}) \propto \prod_{i=1}^N p(\mathbf{y}_i | \mathbf{f}_i, d_i) p(\mathbf{f}_i | d_i, \mathbf{Y}_{1:i-1}) p(d_i) \propto \prod_{i=1}^N \mathcal{N}(\mathbf{f}_i | \hat{\mathbf{f}}_i, d_i^2 \tilde{\mathbf{K}}_i) \mathcal{IG}(d_i^2 | \tilde{\alpha}_i, \tilde{\beta}_i), \quad (17)$$

where $\tilde{\mathbf{K}}_i = \mathbf{K}_i - \mathbf{K}_i \mathbf{G}_i^{-1} \mathbf{K}_i$ and $\hat{\mathbf{f}}_i = \mathbf{K}_i \mathbf{G}_i^{-1} \mathbf{y}_i$.

Writing $\mathbf{f}^* = (f_1^*, \dots, f_N^*)^\top$, $f_i^* = f_i(\mathbf{y}_{1:i-1}^*)$, we have $p(\mathbf{y}^* | \mathbf{f}^*, \mathbf{d}) = \prod_{i=1}^N \mathcal{N}(y_i^* | f_i^*, d_i^2)$ using (4), and $p(\mathbf{f}^* | \mathbf{F}, \mathbf{d}) = \prod_{i=1}^N p(f_i^* | \mathbf{f}_i, d_i)$ due to the conditional-independence assumption in (7). Combining this with (17), we can write the posterior predictive distribution as

$$p(\mathbf{y}^* | \mathbf{Y}) = \iiint p(\mathbf{y}^* | \mathbf{f}^*, \mathbf{d}) p(\mathbf{f}^* | \mathbf{F}, \mathbf{d}) p(\mathbf{F}, \mathbf{d} | \mathbf{Y}) d\mathbf{f}^* d\mathbf{F} d\mathbf{d} = \prod_{i=1}^N \int p(y_i | \mathbf{y}_{1:i-1}^*, \mathbf{Y}, d_i) p(d_i | \mathbf{Y}) dd_i,$$

where basic GP regression implies

$$y_i^* | \mathbf{y}_{1:i-1}^*, \mathbf{Y}, d_i \sim \mathcal{N}(\hat{f}_i(\mathbf{y}_{1:i-1}^*), d_i^2 (v_i(\mathbf{y}_{1:i-1}^*) + 1)), \quad i = 1, \dots, N.$$

Combining this with $d_i^2 | \mathbf{Y} \sim \mathcal{IG}(\tilde{\alpha}_i, \tilde{\beta}_i)$ from (17), we obtain the posterior predictive distribution as a product of t densities,

$$p(\mathbf{y}^* | \mathbf{Y}) = \prod_{i=1}^N t_{2\tilde{\alpha}_i}(y_i^* | \hat{f}_i(\mathbf{y}_{1:i-1}^*), \hat{d}_i^2 (v_i(\mathbf{y}_{1:i-1}^*) + 1)), \quad (18)$$

where our notation is such that $w \sim t_\kappa(\mu, \sigma^2)$ implies that $(w - \mu)/\sigma$ follows a “standard” t with κ degrees of freedom. Hence, $\hat{d}_i^{-1} (v_i(\mathbf{y}_{1:i-1}^*) + 1)^{-1/2} (y_i^* - \hat{f}_i(\mathbf{y}_{1:i-1}^*))$ follows a $t_{2\tilde{\alpha}_i}$ distribution. Using the fact that we can map from a distribution to the standard uniform using its cumulative distribution, the transformation $\mathbf{z}^* = \tilde{\mathcal{T}}(\mathbf{y}^*) \sim \mathcal{N}_N(\mathbf{0}, \mathbf{I}_N)$ to a standard normal can be described using a triangular map with components

$$z_i^* = \tilde{\mathcal{T}}_i(y_1^*, \dots, y_i^*) = \Phi^{-1}(F_{2\tilde{\alpha}_i}(\hat{d}_i^{-1} (v_i(\mathbf{y}_{1:i-1}^*) + 1)^{-1/2} (y_i^* - \hat{f}_i(\mathbf{y}_{1:i-1}^*))))). \quad (19)$$

The solution \mathbf{y}^* to the nonlinear triangular system $\tilde{\mathcal{T}}(\mathbf{y}^*) = \mathbf{z}^*$ can be found recursively by simply solving (19) for y_i^* :

$$y_i^* = F_{2\tilde{\alpha}_i}^{-1}(\Phi(z_i^*)) \hat{d}_i(v_i(\mathbf{y}_{1:i-1}^*) + 1)^{1/2} + \hat{f}_i(\mathbf{y}_{1:i-1}^*).$$

□

Proof of Proposition 2. From (7), we have that $\mathbf{f}_i|d_i \stackrel{ind.}{\sim} \mathcal{N}_n(\mathbf{0}, d_i^2 \mathbf{K}_i)$; together with (16), this implies that $\mathbf{y}_i|d_i, \mathbf{Y}_{1:i-1} \stackrel{ind.}{\sim} \mathcal{N}_n(\mathbf{0}, d_i^2 \mathbf{G}_i)$. Combining this with (6), it is well known that $\mathbf{y}_i|\mathbf{Y}_{1:i-1} \stackrel{ind.}{\sim} t_{2\alpha_i}(\mathbf{0}, \frac{\beta_i}{\alpha_i} \mathbf{G}_i)$, where we define a multivariate t distribution such that $\mathbf{w} \sim t_\kappa(\boldsymbol{\mu}, \boldsymbol{\Sigma})$ implies that the entries of $\boldsymbol{\Sigma}^{-1/2}(\mathbf{w} - \boldsymbol{\mu})$ are iid standard t with κ degrees of freedom. Plugging in the t densities and simplifying using $\tilde{\alpha}_i = \alpha_i + n/2$, $\tilde{\beta}_i = \beta_i + \mathbf{y}_i^\top \mathbf{G}_i^{-1} \mathbf{y}_i/2$, we can obtain

$$\begin{aligned} p(\mathbf{Y}) &= \prod_{i=1}^N t_{2\alpha_i}(\mathbf{y}_i|\mathbf{0}, \frac{\beta_i}{\alpha_i} \mathbf{G}_i) \\ &\propto \prod_{i=1}^N \Gamma(\tilde{\alpha}_i) (\Gamma(\alpha_i) (\alpha_i \beta_i / \alpha_i)^{n/2} |\mathbf{G}_i|^{1/2})^{-1} (1 + \alpha_i / (\beta_i 2\alpha_i) \mathbf{y}_i^\top \mathbf{G}_i^{-1} \mathbf{y}_i)^{-\tilde{\alpha}_i} \\ &\propto \prod_{i=1}^N (|\mathbf{G}_i|^{-1/2} \times (\beta_i^{\alpha_i} / \tilde{\beta}_i^{\tilde{\alpha}_i}) \times \Gamma(\tilde{\alpha}_i) / \Gamma(\alpha_i)), \end{aligned}$$

where $\Gamma(\cdot)$ denotes the gamma function. □

B Conditional near-Gaussianity for quasi-quadratic log-likelihoods

A Gaussian process with precision operator A and mean μ has a quadratic negative loglikelihood given by $u \mapsto \frac{1}{2} \langle u, Au \rangle - \langle b, u \rangle$, with $b = A\mu$. It is therefore closely related to the solution of systems of equation in A . For many popular smooth function priors, such as the Matérn process, the precision operator is a linear elliptic partial differential operator. Just like the linear system $Au = b$ is associated with the minimization of the energy $u \mapsto \frac{1}{2} \langle u, Au \rangle - \langle b, u \rangle$, many quasilinear partial differential equations of the form

$$L(D^s u) + V(D^{s-1} u, \dots, u) = 0, \quad (20)$$

with L linear and V possibly nonlinear, are associated with the minimization of the quasiquadratic energy

$$\mathcal{E}(u) = \langle u, L(D^s u) \rangle + \langle u, V(D^{s-1} u, \dots, u) \rangle.$$

A natural stochastic model for phenomena governed by (20) is then the Boltzmann distribution at a finite temperature T ; not concerning ourselves with the technical difficulties of a rigorous definition in the continuous case, the distribution has the likelihood

$$p(u) \propto \exp(-\mathcal{E}(u)/T). \quad (21)$$

Cahn and Hilliard (1958) derived expressions of the form

$$\mathcal{E}(u) = \int \nu |\nabla u(x)|^2 + (1 - u(x)^2)^2 dx \quad (22)$$

for the free energy of a binary alloy, which has subsequently been applied to numerous other problems including multi-phase flows (Badalassi et al., 2003) and polymers (Choksi et al., 2009). We will use this energy and the associated Boltzmann distribution as an example to illustrate the conditional Gaussianity stochastic processes with quasiquadratic loglikelihoods.

In (22), the field u represents a mixture of two species. The first, leading term of $\mathcal{E}(u)$ favors smooth functions, by preventing drastic jumps in concentration among nearby points. The second term of $\mathcal{E}(u)$ describes a tendency of the two species to avoid mixing, favouring $u(x) = -1$ (mostly the first species) or $u(x) = 1$ (mostly the second species). When imposing the constraint that the overall abundance of the two species be equal ($\int u dx = 0$), minimizers of \mathcal{E} need to carefully balance having values close to $\{-1, 1\}$ while also varying slowly in space, resulting in the formation of distinct positive or negative regions, the size of

which is determined by the choice of ν . For each x , the distribution of $u(x)$ is then a mixture of the behavior of a positive region and that of a negative region, leading to a non-Gaussian marginal distribution. If, however, we condition the process on averages over subdomains of order $\ell < 1$, we observe that the conditional distributions quickly become Gaussian. The intuitive explanation for this phenomenon is that these averages contain enough information to determine, with high probability, whether a given point is part of a positive or negative region. Thus, its conditional distribution is dominated by the approximately Gaussian fluctuation around either a positive or negative value, as opposed to a mixture of these two distributions. In Figure 3, we used the preconditioned Crank-Nicholson proposal (Cotter et al., 2013) to simulate draws from such a Cahn-Hilliard process on a grid of 64×64 locations and plot the standardized histogram for a single location. Our experimental results confirm our intuition that conditioning on averages over fine scales leads to increasingly Gaussian conditional distributions.

This phenomenon can be understood in terms of the well-known Poincaré inequality (Adams and Fournier, 2003, Theorem 4.12):

LEMMA 1 (Poincaré inequality). *Let $\Omega \subset \mathbb{R}^d$ be a Lipschitz-bounded domain with diameter ℓ , let u and its first derivative be square-integrable, and let $u_\Omega = \frac{1}{|\Omega|} \int_\Omega u(x)dx$ be the mean of u over Ω . Then, we have*

$$\|u - u_\Omega\|_{L^2(\Omega)} \leq \ell \|\nabla u\|_{L^2(\Omega)}.$$

The Poincaré inequality implies that conditional on averages over domains of diameter ℓ , perturbations of u with L^2 -norm δ will necessarily lead to perturbations of ∇u with L^2 -norm δ/ℓ . As ℓ decreases, the quadratic leading-order term thus becomes the dominant contribution to the log-likelihood and accordingly the conditional distribution is approximately Gaussian. (To control the contribution of the nonlinearity, we need to bound the L^4 norm, as well as the L^2 norm. For $d \leq 3$, Ladyzhenskaya’s inequality allows us to bound the L^4 norm in terms of the L^2 norm, using the fact that the Sobolev norm H^1 norm of u is small, with high probability.)

The Cahn-Hilliard process is too rough for point-wise measurements to be defined, which is why we have used the conditioning on averages of scale $\ell \approx \ell^k$ as a substitute for conditioning on the first k elements in the maximin ordering introduced in Section 3.1. If the order s of the elliptic PDE is larger than the spatial dimension d , and thus pointwise measurements are well-defined, estimates similar to Madych and Potter (1985, Lemma 1 and Theorem 1) can be used instead of the Poincaré inequality to obtain similar results when conditioning on subsampled data. (See Owhadi and Scovel (2017); Schäfer et al. (2021b) for examples in the Gaussian case).

C Gibbs sampler for Dirichlet process mixture model

The model in Section 4 can be fitted using a Gibbs sampler with some Metropolis-Hasting steps.

This requires additional notation. We introduce cluster indicators $\mathbf{c}_i = (c_i^{(1)}, \dots, c_i^{(n)})$, such that $c_i^{(j)}$ indicates the cluster to which $\epsilon_i^{(j)}$ belongs. We denote by n_i the number of clusters (i.e., the number of unique entries of \mathbf{c}_i). Further, let $\tilde{\boldsymbol{\mu}}_i$ and $\tilde{\mathbf{d}}_i$ contain the n_i unique cluster-specific parameters in $(\mu_i^{(1)}, \dots, \mu_i^{(n)})$ and $(d_i^{(1)}, \dots, d_i^{(n)})$, respectively; for example, we have $\mu_i^{(j)} = \tilde{\mu}_{i, c_i^{(j)}}$.

For each cluster $k = 1, \dots, n_i$, consider the within-cluster index set $\mathcal{J}_{i,k} = \{l : c_i^{(l)} = k\}$, the cluster size $n_{i,k} = |\mathcal{J}_{i,k}|$, and the cluster average $\bar{\epsilon}_{i,k} = (1/n_{i,k}) \sum_{l \in \mathcal{J}_{i,k}} \epsilon_i^{(l)}$. Then, define $\tilde{\xi}_{i,k} = (\eta_i \xi_i + n_{i,k} \bar{\epsilon}_{i,k}) / \tilde{\eta}_{i,k}$, $\tilde{\eta}_{i,k} = \eta_i + n_{i,k}$, $\tilde{\alpha}_{i,k} = \alpha_i + n_{i,k}/2$, and $\tilde{\beta}_{i,k} = \beta_i + (1/2) \sum_{l \in \mathcal{J}_{i,k}} (\epsilon_i^{(l)} - \bar{\epsilon}_{i,k})^2 + (1/2) n_{i,k} \eta_i (\bar{\epsilon}_{i,k} - \xi_i)^2 / \tilde{\eta}_{i,k}$. Further, let $\tilde{\xi}_{i,k}^{(-j)}$, $\tilde{\eta}_{i,k}^{(-j)}$, $\tilde{\alpha}_{i,k}^{(-j)}$, and $\tilde{\beta}_{i,k}^{(-j)}$ be the corresponding quantities computed without $\epsilon_i^{(j)}$.

We propose a Markov chain Monte Carlo (MCMC) procedure that, after initialization, cycles through the following steps for a large number of iterations:

1. For $i = 1, \dots, N$, sample $\boldsymbol{\epsilon}_i | \mathbf{Y}, \tilde{\boldsymbol{\mu}}_i, \tilde{\mathbf{d}}_i, \mathbf{c}_i, \boldsymbol{\theta}$ from $\mathcal{N}_n(\hat{\boldsymbol{\epsilon}}_i, \mathbf{D}_i - \mathbf{D}_i \mathbf{G}_i^{-1} \mathbf{D}_i)$, where $\hat{\boldsymbol{\epsilon}}_i = \boldsymbol{\mu}_i + \mathbf{D}_i \mathbf{G}_i^{-1} (\mathbf{y}_i - \boldsymbol{\mu}_i)$, $\mathbf{G}_i = \mathbf{C}_i + \mathbf{D}_i$, $\mathbf{D}_i = \text{diag}((d_i^{(1)})^2, \dots, (d_i^{(n)})^2)$, and $\mathbf{C}_i = C_i(\mathbf{Y}_{1:i-1}, \mathbf{Y}_{1:i-1})$ depends on $\boldsymbol{\theta}$.
2. For $i = 1, \dots, N$, sequentially sample $c_i^{(1)}, \dots, c_i^{(n)}$ from $p(\mathbf{c}_i | \boldsymbol{\epsilon}_i, \boldsymbol{\theta}) \propto \prod_{j=1}^n p(c_i^{(j)} | \mathbf{c}_i^{(-j)}, \boldsymbol{\epsilon}_i, \boldsymbol{\theta})$ with $\tilde{\boldsymbol{\mu}}_i, \tilde{\mathbf{d}}_i$ integrated out (MacEachern, 1994; Neal, 2000). Specifically, we have $P(c_i^{(j)} = k | \mathbf{c}_i^{(-j)}, \boldsymbol{\epsilon}_i, \boldsymbol{\theta}) \propto$

$\frac{n_{i,k}^{(j)}}{n-1+\zeta_i} b_{i,k}^{(j)}$ for $k = 1, \dots, n_i+1$, where $n_{i,n_i+1} = \zeta_i$ and $b_{i,k}^{(j)} = p(\epsilon_i^{(j)} | \epsilon_i^{(-j)}, \boldsymbol{\theta}) = t_{2\tilde{\alpha}_{i,k}^{(-j)}}(\tilde{\xi}_{i,k}^{(-j)}, \frac{\tilde{\beta}_{i,k}^{(-j)}(\tilde{\eta}_{i,k}^{(-j)}+1)}{\tilde{\alpha}_{i,k}^{(-j)}\tilde{\eta}_{i,k}^{(-j)}})$ is the density of a nonstandardized t distribution.

3. For $i = 1, \dots, N$, sample $(\tilde{\mu}_{i,k}, \tilde{d}_{i,k}^2)$ from $p(\tilde{\mu}_i, \tilde{\mathbf{d}}_i^2 | \boldsymbol{\epsilon}_i, \mathbf{c}_i, \boldsymbol{\theta}) = \prod_{k=1}^{n_i} \mathcal{NIG}(\tilde{\mu}_{i,k}, \tilde{d}_{i,k}^2 | \tilde{\xi}_{i,k}, \tilde{\eta}_{i,k}, \tilde{\alpha}_{i,k}, \tilde{\beta}_{i,k})$.
4. Using Metropolis-Hastings, sample $\boldsymbol{\theta}$ from

$$p(\boldsymbol{\theta} | \{\mathbf{y}_i, \mathbf{c}_i, \boldsymbol{\epsilon}_i, \tilde{\mu}_i, \tilde{\mathbf{d}}_i^2 : i = 1, \dots, N\}) = p(\boldsymbol{\theta}_\zeta | \{\mathbf{c}_i\}) p(\boldsymbol{\theta}_\sigma, \boldsymbol{\theta}_\gamma, \boldsymbol{\theta}_q | \{\mathbf{y}_i, \boldsymbol{\epsilon}_i\}) p(\boldsymbol{\theta}_d, \boldsymbol{\theta}_\eta | \{\tilde{\mu}_i, \tilde{\mathbf{d}}_i^2\}) \\ \propto (\prod_{i=1}^N \zeta_i^{n_i} \Gamma(\zeta_i) / \Gamma(n + \zeta_i)) (\prod_{i=1}^N \mathcal{N}_n(\mathbf{y}_i - \boldsymbol{\epsilon}_i | \mathbf{0}, \mathbf{C}_i)) (\prod_{i=1}^N \prod_{j=1}^{n_i} \mathcal{NIG}(\tilde{\mu}_{i,k}, \tilde{d}_{i,k}^2 | \xi_i, \eta_i, \alpha_i, \beta_i)),$$

where each of the product terms depend on different components of $\boldsymbol{\theta}$, which we thus sample and accept/reject separately.

Steps 1–3 can be carried out in parallel for $i = 1, \dots, N$; for Step 4, the terms for $i = 1, \dots, N$ can also be computed in parallel and then combined to obtain the acceptance probabilities for new values of $\boldsymbol{\theta}$.

The posterior predictive distribution for a new observation \mathbf{y}^* can be written as

$$p(\mathbf{y}^* | \mathbf{Y}) = \prod_{i=1}^N p(y_i^* | \mathbf{y}_{1:i-1}^*, \mathbf{Y}),$$

for which each $p(y_i^* | \mathbf{y}_{1:i-1}^*, \mathbf{Y})$ is approximated as a mixture of Gaussians based on the MCMC output from above. More precisely, given L (potentially thinned) samples of the state variables from the Gibbs sampler, we have

$$p(y_i^* | \mathbf{y}_{1:i-1}^*, \mathbf{Y}) = (1/L) \sum_{l=1}^L \sum_{k=1}^{n_i+1} w_{i,k}^{(l)} \mathcal{N}(y_i^* | f_i^{(l)}(\mathbf{y}_{1:i-1}^*), \tilde{\mu}_{i,k}^{(l)} v_i^{(l)}(\mathbf{y}_{1:i-1}^*) + (\tilde{d}_{i,k}^{(l)})^2),$$

where $w_{i,k}^{(l)} = n_{i,k}^{(l)} / (n_i^{(l)} + \zeta_i^{(l)})$, $f_i^{(l)}(\mathbf{y}_{1:i-1}^*) = C_i^{(l)}(\mathbf{y}_{1:i-1}^*, \mathbf{Y}_{1:i-1}) (\mathbf{G}_i^{(l)})^{-1} \mathbf{y}_i$, $v_i^{(l)}(\mathbf{y}_{1:i-1}^*) = C_i^{(l)}(\mathbf{y}_{1:i-1}^*, \mathbf{Y}_{1:i-1}) - C_i^{(l)}(\mathbf{y}_{1:i-1}^*, \mathbf{Y}_{1:i-1}) (\mathbf{G}_i^{(l)})^{-1} C_i^{(l)}(\mathbf{Y}_{1:i-1}, \mathbf{y}_{1:i-1}^*)$, and $(\tilde{\mu}_{i,n_i+1}^{(l)}, (\tilde{d}_{i,n_i+1}^{(l)})^2) \sim \mathcal{NIG}(\xi_i^{(l)}, \eta_i^{(l)}, \alpha_i^{(l)}, \beta_i^{(l)})$.

References

- Adams, R. A. and Fournier, J. J. F. (2003). *Sobolev spaces*, volume 140 of *Pure and Applied Mathematics (Amsterdam)*. Elsevier/Academic Press, Amsterdam, second edition.
- Allen, S. M. and Cahn, J. W. (1972). Ground state structures in ordered binary alloys with second neighbor interactions. *Acta Metallurgica*, 20(3):423–433.
- Badalassi, V. E., Cenicerros, H. D., and Banerjee, S. (2003). Computation of multiphase systems with phase field models. *Journal of Computational Physics*, 190(2):371–397.
- Banerjee, S., Carlin, B. P., and Gelfand, A. E. (2004). *Hierarchical Modeling and Analysis for Spatial Data*. Chapman & Hall.
- Baptista, R., Zahm, O., and Marzouk, Y. (2020). An adaptive transport framework for joint and conditional density estimation. *arXiv preprint arXiv:2009.10303*.
- Benestad, R., Sillmann, J., Thorarinsdottir, T. L., Guttorp, P., Mesquita, M. D., Tye, M. R., Uotila, P., Maule, C. F., Thejll, P., Drews, M., and Parding, K. M. (2017). New vigour involving statisticians to overcome ensemble fatigue. *Nature Climate Change*, 7(10):697–703.
- Bigoni, D., Spantini, A., and Marzouk, Y. (2016). Adaptive construction of measure transports for Bayesian inference. In *NIPS 2016 workshop on Advances in Approximate Bayesian Inference*.
- Bolin, D. and Wallin, J. (2020). Multivariate type G Matérn stochastic partial differential equation random fields. *Journal of the Royal Statistical Society, Series B*.
- Boyles, W. and Katzfuss, M. (2021). Ensemble Kalman filter updates based on regularized sparse inverse Cholesky factors. *Monthly Weather Review*, 149(7):2231–2238.
- Cahn, J. W. and Hilliard, J. E. (1958). Free energy of a nonuniform system. I. Interfacial free energy. *The Journal of Chemical Physics*, 28(2):258–267.
- Carlier, G., Galichon, A., and Santambrogio, F. (2009). From Knothe’s transport to Brenier’s map and a continuation method for optimal transport. *SIAM Journal on Mathematical Analysis*, 41(6):2554–2576.

- Castruccio, S., McInerney, D. J., Stein, M. L., Crouch, F. L., Jacob, R. L., and Moyer, E. J. (2014). Statistical emulation of climate model projections based on precomputed GCM runs. *Journal of Climate*, 27(5):1829–1844.
- Castruccio, S. and Stein, M. L. (2013). Global space-time models for climate ensembles. *Annals of Applied Statistics*, 7(3):1593–1611.
- Choi, I. K., Li, B., and Wang, X. (2013). Nonparametric estimation of spatial and space-time covariance function. *Journal of Agricultural, Biological, and Environmental Statistics*, 18(4):611–630.
- Choksi, R., Peletier, M. A., and Williams, J. (2009). On the phase diagram for microphase separation of diblock copolymers: an approach via a nonlocal Cahn–Hilliard functional. *SIAM Journal on Applied Mathematics*, 69(6):1712–1738.
- Cotter, S. L., Roberts, G. O., Stuart, A. M., and White, D. (2013). MCMC methods for functions: modifying old algorithms to make them faster. *Statistical Science*, 28(3):424–446.
- Cressie, N. (1993). *Statistics for Spatial Data, revised edition*. John Wiley & Sons, New York, NY.
- Datta, A., Banerjee, S., Finley, A. O., and Gelfand, A. E. (2016). Hierarchical nearest-neighbor Gaussian process models for large geostatistical datasets. *Journal of the American Statistical Association*, 111(514):800–812.
- El Moselhy, T. A. and Marzouk, Y. M. (2012). Bayesian inference with optimal maps. *Journal of Computational Physics*, 231(23):7815–7850.
- Gelfand, A. E. and Schliep, E. M. (2016). Spatial statistics and Gaussian processes: A beautiful marriage. *Spatial Statistics*, 18(A):86–104.
- Gneiting, T. and Katzfuss, M. (2014). Probabilistic forecasting. *Annual Review of Statistics and Its Application*, 1(1):125–151.
- Goodfellow, I., Bengio, Y., and Courville, A. (2016). *Deep Learning*. MIT Press.
- Gräler, B. (2014). Modelling skewed spatial random fields through the spatial vine copula. *Spatial Statistics*, 10:87–102.
- Guinness, J. (2018). Permutation and grouping methods for sharpening Gaussian process approximations. *Technometrics*, 60(4):415–429.
- Haugen, M. A., Stein, M. L., Sriver, R. L., and Moyer, E. J. (2019). Future climate emulations using quantile regressions on large ensembles. *Advances in Statistical Climatology, Meteorology, and Oceanography*, 5:37–55.
- Huang, C., Hsing, T., and Cressie, N. (2011). Nonparametric estimation of the variogram and its spectrum. *Biometrika*, 98(4):775–789.
- Katzfuss, M. and Guinness, J. (2021). A general framework for Vecchia approximations of Gaussian processes. *Statistical Science*, 36(1):124–141.
- Katzfuss, M., Guinness, J., Gong, W., and Zilber, D. (2020a). Vecchia approximations of Gaussian-process predictions. *Journal of Agricultural, Biological, and Environmental Statistics*, 25(3):383–414.
- Katzfuss, M., Guinness, J., and Lawrence, E. (2020b). Scaled Vecchia approximation for fast computer-model emulation. *arXiv:2005.00386*.
- Kay, J. E., Deser, C., Phillips, A., Mai, A., Hannay, C., Strand, G., Arblaster, J. M., Bates, S. C., Danabasoglu, G., Edwards, J., Holland, M., Kushner, P., Lamarque, J. F., Lawrence, D., Lindsay, K., Middleton, A., Munoz, E., Neale, R., Oleson, K., Polvani, L., and Vertenstein, M. (2015). The Community Earth System Model (CESM) Large Ensemble Project: A community resource for studying climate change in the presence of internal climate variability. *Bulletin of the American Meteorological Society*, 96(8):1333–1349.
- Kidd, B. and Katzfuss, M. (2021). Bayesian nonstationary and nonparametric covariance estimation for large spatial data. *Bayesian Analysis*, accepted.
- Kobyzev, I., Prince, S., and Brubaker, M. (2020). Normalizing flows: An introduction and review of current methods. *IEEE Transactions on Pattern Analysis and Machine Intelligence*.
- Kovachki, N. B., Hosseini, B., Baptista, R., and Marzouk, Y. M. (2020). Conditional sampling with monotone GANs. *arXiv:2006.06755*.
- Krupskii, P., Huser, R., and Genton, M. G. (2018). Factor copula models for replicated spatial data. *Journal*

- of the American Statistical Association, 113(521):467–479.
- MacEachern, S. N. (1994). Estimating normal means with a conjugate style Dirichlet process prior. *Communications in Statistics - Simulation and Computation*, 23(3):727–741.
- Madych, W. and Potter, E. (1985). An estimate for multivariate interpolation. *Journal of Approximation Theory*, 43(2):132–139.
- Marzouk, Y. M., Moselhy, T., Parno, M., and Spantini, A. (2016). Sampling via measure transport: An introduction. In Ghanem, R., Higdon, D., and Owhadi, H., editors, *Handbook of Uncertainty Quantification*. Springer.
- Neal, R. M. (2000). Markov chain sampling methods for Dirichlet process mixture models. *Journal of Computational and Graphical Statistics*, 9(2):249.
- Nychka, D. W., Hammerling, D., Krock, M., and Wiens, A. (2018). Modeling and emulation of nonstationary Gaussian fields. *Spatial Statistics*, 28:21–38.
- Owhadi, H. and Scovel, C. (2017). Universal scalable robust solvers from computational information games and fast eigenspace adapted multiresolution analysis. *arXiv preprint arXiv:1703.10761*.
- Porcu, E., Bissiri, P. G., Tagle, F., and Quintana, F. (2019). Nonparametric Bayesian modeling and estimation of spatial correlation functions for global data. *Tech Report*.
- Risser, M. D. (2016). Review: Nonstationary spatial modeling, with emphasis on process convolution and covariate-driven approaches. *arXiv:1610.02447*.
- Rosenblatt, M. (1952). Remarks on a multivariate transformation. *The Annals of Mathematical Statistics*, 23(3):470–472.
- Schäfer, F., Katzfuss, M., and Owhadi, H. (2021a). Sparse Cholesky factorization by Kullback-Leibler minimization. *SIAM Journal on Scientific Computing*, 43(3):A2019–A2046.
- Schäfer, F., Sullivan, T. J., and Owhadi, H. (2021b). Compression, inversion, and approximate PCA of dense kernel matrices at near-linear computational complexity. *Multiscale Modeling & Simulation*, 19(2):688–730.
- Spantini, A., Bigoni, D., and Marzouk, Y. (2018). Inference via low-dimensional couplings. *Journal of Machine Learning Research*, 19(1).
- Stein, M. L. (2011). 2010 Rietz lecture: When does the screening effect hold? *The Annals of Statistics*, 39(6):2795–2819.
- Stein, M. L., Chi, Z., and Welty, L. (2004). Approximating likelihoods for large spatial data sets. *Journal of the Royal Statistical Society: Series B*, 66(2):275–296.
- Vecchia, A. (1988). Estimation and model identification for continuous spatial processes. *Journal of the Royal Statistical Society, Series B*, 50(2):297–312.
- Villani, C. (2009). *Optimal Transport: Old and New*. Springer.
- Wallin, J. and Bolin, D. (2015). Geostatistical modelling using non-Gaussian Matérn fields. *Scandinavian Journal of Statistics*, 42(3):872–890.
- Whittle, P. (1954). On stationary processes in the plane. *Biometrika*, 41:434–449.
- Whittle, P. (1963). Stochastic processes in several dimensions. *Bulletin of the International Statistical Institute*, 40(2):974–994.
- Xu, G. and Genton, M. G. (2017). Tukey g-and-h Random Fields. *Journal of the American Statistical Association*, 112(519):1236–1249.